Geophysical Journal International

Geophys. J. Int. (2026) **244,** 1–24
Advance Access publication 2025 December 5
Review Paper

https://doi.org/10.1093/gji/ggaf489

Fibre-optic exploration of the cryosphere

Andreas Fichtner [1], Fabian Walter,[2,3] Alex Brisbourne,[4] Adam D. Booth,[5] John Michael Kendall,[6] Thomas Hudson [1], Patrick Paitz[2] and Bradley Paul Lipovsky[7]

[1] *Department of Earth and Planetary Sciences, ETH Zurich,* 8092 *Zurich, Switzerland. E-mail: andreas.fichtner@eaps.ethz.ch*
[2] *Swiss Federal Research Institute WSL,* 8903 *Birmensdorf, Switzerland*
[3] *Laboratory of Hydraulics, Hydrology and Glaciology VAW, ETH Zurich,* 8093 *Zurich, Switzerland*
[4] *Ice Dynamics and Palaeoclimate, British Antarctic Survey, Cambridge CB3 0ET, UK*
[5] *School of Earth and Environment, University of Leeds, Leeds LS2 9JT, UK*
[6] *Department of Earth Sciences, University of Oxford, Oxford OX1 3AN, UK*
[7] *Department of Earth and Space Sciences, University of Washington, Seattle, WA* 98195-1310, *USA*

Accepted 2025 November 20. Received 2025 November 19; in original form 2025 June 21

SUMMARY

The icy parts of the Earth, known as the cryosphere, are an integral part of the climate system. Comprehensively understanding the cryosphere requires dense observations, not only of its surface, but also of its internal structure and dynamics. Seismic methods play a central role in this endeavour. Fibre-optic sensing is emerging as a valuable complement and alternative to well-established inertial seismometers. Offering metre-scale channel spacing, interrogation distances of up to ∼100 km and a bandwidth from mHz to kHz, it has enabled new seismological applications, for instance, under water, in cities and on volcanoes. Cryosphere research particularly benefits from fibre-optic sensing because long cables can be deployed with relative ease in icy environments where dense arrays of seismometers are difficult to install, including glaciers, ice sheets and deep boreholes. Intended to facilitate future fibre-optic seismology research in the cryosphere, this *Expository Review* combines a classical publication review with theoretical background, a practical field guide, a cryospheric signal gallery and open-access data examples for hands-on training. Following a summary of recent findings about firn and ice structure, glacial seismicity, hydrology and avalanche dynamics, we derive the ideal instrument response of a distributed fibre-optic deformation sensor. To approach this ideal in field experiments, we propose numerous practical dos and don'ts concerning the choice and handling of fibre-optic cables, required equipment, splicing in the field at low temperatures, cable layout and trenching, and the deployment and coupling of cables in boreholes. A cryospheric signal gallery provides examples of data from a wide range of sources, such as explosions, land and air traffic, electricity generators, basal stick-slip icequakes, surface crevassing, englacial icequake cascades, floating ice shelf resonance, surface water flow and snow avalanches. Many of these data are enclosed as an open-access training resource, together with code for reading, visualization and simple analyses. This review concludes with a discussion of grand open challenges in our understanding of cryosphere structure and dynamics, and how further advances in fibre-optic sensing may help to overcome them.

Key words: Glaciology; Distributed acoustic sensing; Seismic instruments; Wave propagation.

1 INTRODUCTION

The cryosphere is the part of the Earth's surface where water exists in solid form. It comprises the Antarctic and Greenlandic ice sheets, numerous ice caps and glaciers, sea and lake ice, snow and permafrost. Through complex interactions with the hydro-, atmo-, litho- and biospheres, the cryosphere is an integral part of the Earth's climate system. At the same time, it both enables life as we know it and poses existential threats.

1.1 Seismic waves as carriers of information on cryosphere processes

By 2050, around one billion people living in coastal communities are likely to be affected by extreme sea level rise (IPCC 2023). Uncertainties in sea level rise predictions are on the order of several metres over the next ∼200 yr (Seroussi *et al.* 2024). They are dominated by poor constraints on two phenomena that control the ice loss of glaciers and ice sheets: glacier slip and hydrofracture crevassing

(e.g. Pollard *et al.* 2015b; Joughin *et al.* 2019; Oppenheimer *et al.* 2019). While these processes are difficult to observe directly, for example, with satellites, they generate seismic waves that carry invaluable information about their prevalence and potential impact on the dynamics of ice bodies.

A wide variety of additional cryospheric processes of considerable societal importance manifest themselves through the emission of seismic signals. While some of these are illustrated in Section 4, more comprehensive accounts can be found in the review articles by Podolskiy & Walter (2016) and Aster & Winberry (2017). Here, we restrict ourselves to a concise overview: Ice shelves and other floating ice masses give rise to a rich spectrum of seismic wave propagation modes, which encode valuable information about the dynamic interactions between the ice, the underlying ocean and the overlying atmosphere. Such interactions can ultimately foster the detachment of icebergs, whose dimensions may in turn be inferred from the seismic radiation accompanying their calving. On glaciers, the flow of water through englacial and subglacial conduits often constitutes the dominant source of ambient seismic noise during the warmer seasons. Analysis of this noise provides insight into the spatial configuration of subglacial drainage channels as well as estimates of meltwater discharge, a key driver of ice mass loss. Snow avalanches similarly generate seismic signals, which can be detected prior to the arrival of the avalanche itself, thereby offering a foundation for early-warning systems. Beyond naturally occurring sources, anthropogenic seismic signals remain among our most important tools for probing the internal mechanical structure and deformation behaviour of ice bodies.

1.2 Filling observational gaps with fibre-optic sensing

The remoteness and harsh environmental conditions of most of the cryosphere complicate seismic experiments and create a large data gap, similar to the one in the oceans. In both the cryosphere and the oceans, emerging fibre-optic sensing technologies offer the opportunity to reduce this data gap. They are based on measurements of phase or polarization changes of laser light caused by the deformation of an optical fibre through which it propagates. The most widely used technology, distributed acoustic sensing (DAS), effectively transforms a fibre-optic cable into a chain of strain meters. Using fibres with a total length of up to several tens of kilometres, the individual sensors, typically referred to as DAS channels, can have a spacing in the metre range. Comprehensive technical introductions to DAS and reviews of recent seismological applications can be found in Hartog (2017), Zhan (2020), Lindsey & Martin (2021) and Kennett (2024). To provide historical context and illustrate the versatility of DAS, we briefly summarize major application domains that have emerged in recent years.

Some of the earliest applications of DAS were outside the cryosphere and included perimeter security and pipeline monitoring (e.g. Owen *et al.* 2012; Hill 2015), as well as seismic exploration and monitoring with fibre-optic cables installed in boreholes (e.g. Daley *et al.* 2013, 2014, 2016; Mateeva *et al.* 2013, 2014; Dean *et al.* 2016; Hornmann 2017). The large bandwidth of DAS, from mHz to kHz (Lindsey *et al.* 2020; Bernauer *et al.* 2021; Paitz *et al.* 2021), and the possibility of piggy-backing on existing fibre-optic telecommunication infrastructure, opened new opportunities for seismological research in densely populated areas (e.g. Biondi *et al.* 2017; Lindsey *et al.* 2017; Martin *et al.* 2017; Ajo-Franklin *et al.* 2019; Spica *et al.* 2020b; Smolinski *et al.* 2024) and in the oceans (e.g. Sladen *et al.* 2019; Williams *et al.* 2019; Spica *et al.* 2020a; Lior *et al.* 2021; Igel *et al.* 2024). Specially deployed cables in terrain where seismometer networks are difficult to install and maintain provided new insight into the deformation and seismicity of active volcanoes (e.g. Currenti *et al.* 2021; Jousset *et al.* 2022, 2025; Klaasen *et al.* 2022, 2023), the movement of unstable slopes (e.g. Acharya & Kogure 2023; Ouellet *et al.* 2024) and many other phenomena.

1.3 A summary of DAS in cryosphere research

DAS is also starting to transform the field of cryoseismology and has been used successfully to infer diverse glacial processes from seismic wave recordings. Data from a triangle-shaped fibre-optic cable deployed at the surface of Rhône Glacier in the Swiss Alps constrained the locations of basal stick-slip icequakes with an accuracy on the order of 10 m (Walter *et al.* 2020) and contain numerous other seismic signals, for example, from surface crevassing and rock falls, that could potentially be exploited. On Rutford Ice Stream in Antarctica, the dense spatial sampling of DAS data enabled moment tensor inversions for stick-slip icequakes (Butcher *et al.* 2021; Hudson *et al.* 2021) and the reliable measurement of shear-wave splitting caused by ice flow-induced anisotropic fabric. Manos *et al.* (2024) demonstrated that DAS recordings of ambient seismic noise, generated by the flow of melt water, can be used to train machine learning models that predict glacier runoff and outperform standard predictive models based on meteorological data. Unexpected englacial seismic event cascades that propagate vertically over hundreds of metres inside the Northeast Greenland Ice Stream were observed by Fichtner *et al.* (2025), thereby revealing a new internal deformation mode of ice streams.

Fibre-optic cables deployed at the surface provide a low-cost and low-maintenance alternative to core sampling for the high-resolution characterization of firn structure. Data quality of an individual DAS channel may be lower than that of a well-installed geophone, but the dense spatial sampling and long range of DAS enable accurate measurements of surface wave dispersion. Zhou *et al.* (2022) used DAS recordings of ambient seismic noise to infer shear wave velocity structure in the firn layer of Rutford Ice Stream. Fichtner *et al.* (2023b) observed multimode surface waves excited by an airplane landing near the EastGRIP camp on the Northeast Greenland Ice Stream to produce firn velocity profiles with metre-scale vertical resolution. Using similar observations produced by explosive sources, Yang *et al.* (2024) derived a new velocity-density scaling for firn at the South Pole, concluding that previous scaling relations may have underestimated firn air content by over 15 per cent. Going one step further, Lanteri *et al.* (2025) directly constrained firn density on the basis of high-quality multimode surface wave recordings, thereby eliminating the need to apply velocity-density scalings that cannot account for the effect on density of different environmental conditions (e.g. Kohnen 1972; Diez *et al.* 2014).

Below the firn layer, borehole fibre-optic sensing provides constraints on the physical properties of the ice in a volume much larger than that of an ice core. Lowering a fibre-optic cable 1043 m deep into Store Glacier, Greenland, Booth *et al.* (2020) were the first to overcome the challenges of a glacial borehole DAS experiment. Using measurements of P and S waves, they inferred changes in crystal fabric orientation at the Holocene-Wisconsin transition and the presence of temperate ice in the lowermost 100 m of the glacier.

Clearly visible reflected waves evidenced a layer of consolidated sediments at the base up to radial distances of 200 m around the borehole. In a similar experiment at Skytrain Ice Rise, Antarctica, Brisbourne *et al.* (2021) found anomalously high *P*-wave speed caused by strong vertical fabric, but also pointed out that coupling of the fibre to the ice must be improved to constrain variations in crystal preferred orientation. DAS data from the EastGRIP borehole on the Northeast Greenland Ice Stream, analysed by Fichtner *et al.* (2023a), image *P*- and *S*-wave speeds to 1500 m depth with uncertainties of $\sim$10 m s^{-1} and vertical resolution around 50 m. Internally reflected waves reveal the presence of numerous seismic discontinuities at depths that correspond to rapid climatic changes and associated grain size variations.

Mechanical interactions of floating ice with the underlying water body can be measured with fibre-optic sensing and used to constrain a wide range of phenomena and ice properties. Fichtner *et al.* (2022b) observed resonance of the ice sheet floating atop the subglacial lake of Grímsvötn volcano, Iceland and linked it to volcanic microseisms that are too small to be observed without such a natural amplifier. Using a 36 km long seafloor telecommunication cable under the Beaufort Ice Shelf, Smith *et al.* (2023) were able to infer ocean wave attenuation related to sea ice formation, which is an important control on the evolution of Arctic coastlines. With the help of similar data, Peña Castro *et al.* (2023) tracked the local sea ice extent in the Beaufort Sea, providing information with locally higher spatial and temporal resolution than satellite imagery. Using submarine DAS near a calving glacier, Gräff *et al.* (2025) provided new insights into the iceberg calving process. Their observations indicate that calving initiates by sustained ice fracturing, which progressively coalesces into iceberg detachment. This detachment subsequently generates local tsunamis, internal gravity waves and transient currents, before the released icebergs ultimately disintegrate into smaller fragments. DAS deployments on frozen lakes have been used to monitor cracking and estimate ice thickness and elastic moduli (e.g. Nziengui-Bâ *et al.* 2023; Xie *et al.* 2024).

Fibre-optic sensing data are starting to complement optical, radar and infrasound measurements of snow avalanches. Paitz *et al.* (2023) were able to co-use a telecommunication cable deployed in the runout zone of avalanches on a slope of the Vallée de la Sionne avalanche test site in the Swiss Alps. For avalanches propagating approximately along the cable, they obtained high-resolution snapshots of their complex internal structure, including roll waves and multiple secondary surges. Also taking advantage of existing telecommunication infrastructure, Edme *et al.* (2023) demonstrated that snow avalanches close to an Alpine pass road can be detected and characterized, thereby paving the way towards cost-effective, near-real-time avalanche monitoring over long distances (Turquet *et al.* 2024; Kleine *et al.* 2025).

1.4 Purpose and structure of this paper

Fibre-optic sensing for cryospheric research is undergoing rapid development, and its proven potential to contribute new discoveries will likely lead to a multiplication of applications in the future. The primary objective of this paper is to facilitate such applications by offering the necessary theoretical background (Section 2), practical advice for fibre-optic sensing experiments on glaciers and ice sheets (Section 3), a gallery of natural and human-made signals that one may expect (Section 4), a discussion of future research directions and open challenges (Section 5) and a collection of openly accessible data sets and analysis codes for hands-on training (Appendix A).

2 FOUNDATIONS OF DISTRIBUTED FIBRE-OPTIC DEFORMATION SENSING

Fibre-optic deformation sensing rests on the measurement of electromagnetic waves that change their properties in response to deformation of the fibre. These properties include intensity, polarization and phase (e.g. Hartog 2017; Agrawal 2021). Devices that perform such measurements are referred to as interrogators, or in the specific case of DAS as DAS units. The vast majority of seismological applications exploit phase changes of laser light, transmitted either continuously as monochromatic waves, in pulses or chirps; and measured with a wide range of opto-electronic technologies. In the following sections, we take a closer look at different types of optical fibres and cables, derive the ideal response of a distributed fibre-optic sensor to deformation of the fibre and provide a collection of simple numerical examples of such instrument responses. Subsequently, we discuss real-world deviations from the ideal, related to the measurement technology and the coupling of the fibre to the medium of interest.

2.1 Optical fibres and cables

Most DAS interrogators are designed to be used with single-mode fibre (SMF). SMF features a narrow light-carrying core of $\sim$9 μm diameter that allows only one mode of light to propagate. By contrast, multimode fibre (MMF) features a wider light-carrying core, typically between 50 and 100 μm. While MMF supports transmission of multiple light modes that may carry information from emitter to receiver, the transmission distance is limited to a few kilometres. SMF supports propagation along greater distances, currently up to around 100 km, as the transmitted light pulse undergoes less attenuation given reduced internal reflection. Dispersion effects are also minimized, hence the phase of the transmitted pulse is more stable through the cable length. Optical fibres can be embedded in different types of cable constructions that roughly fall into two categories. Loose-tube cables consist of an optical fibre surrounded by a thin film of water-blocking gel and placed inside a hard tube that offers mechanical stability. Loose-tube cables are considered more suitable for distributed temperature sensing (DTS) because they allow the fibre to move more freely in response to thermal expansion and contraction. In contrast, tight-buffered cables contain fibres that are mechanically coupled to the tube by some kind of plastic buffer. This construction results in a more direct strain transfer into the fibre and is therefore often favoured in fibre-optic deformation measurements (e.g. Castongia *et al.* 2017; Forbriger *et al.* 2025).

2.2 The exact and ideal instrument response of a distributed fibre-optic sensor

As a prelude, we consider the reference state where the fibre is initially at rest. At one end of the fibre, an electromagnetic wave is emitted. It propagates across some distance L where it encounters a scatterer. On the one hand, these scatterers may be randomly occurring defects that cannot be avoided in the fabrication process. On the other hand, intense ultraviolet lasers may be used to inscribe a Bragg grating, that is, scatterers at well-defined periodic locations, to produce an engineered fibre. The scattered pulse travels the same

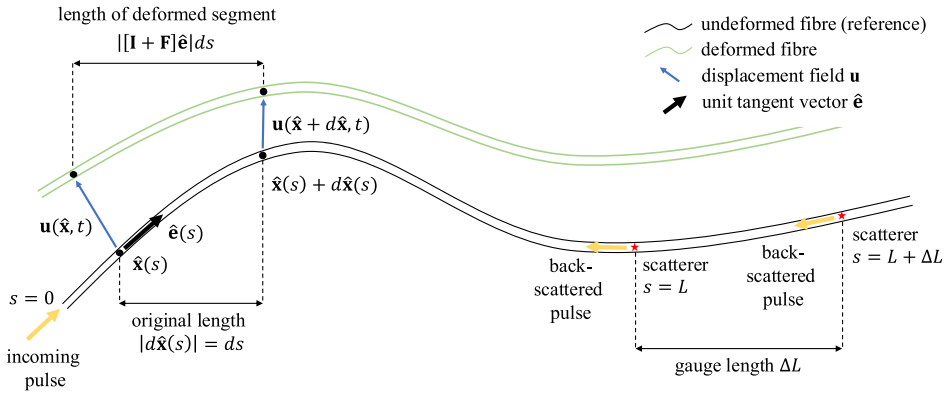

Figure 1. Schematic illustration of a deforming fibre, parametrized in terms of the arc length s. The undeformed reference state is represented by the black fibre, the deformed state by the green fibre. Under deformation, neighbouring material points of the fibre move from $\hat{\mathbf{x}}$ to $\hat{\mathbf{x}}+\mathbf{u}(\hat{\mathbf{x}},t)$ and from $\hat{\mathbf{x}}+\mathrm{d}\hat{\mathbf{x}}$ to $\hat{\mathbf{x}}+\mathrm{d}\hat{\mathbf{x}}+\mathbf{u}(\hat{\mathbf{x}}+\mathrm{d}\hat{\mathbf{x}},t)$, respectively. As a consequence, the length of an infinitesimal fibre segment changes from $\mathrm{d}s$ to $|[\mathbf{I}+\mathbf{F}]\hat{\mathbf{e}}|\mathrm{d}s$, where $\mathbf{F}$ is the deformation tensor with components $F_{ij}=\partial u_i/\partial x_j$. This affects the two-way traveltime of electromagnetic waves that travel from an emitter at the start of the fibre to some scattering point at $s=L$ and back. The differential traveltime with respect to a second scatterer at $s=L+\Delta L$ enables the association of an optical phase change with deformation in the interval $[L, L+\Delta L]$, where ΔL is referred to as the gauge length.

distance L back to the start of the fibre. The geometric setup is shown schematically in Fig.1 We denote the position vector along the fibre by $\hat{\mathbf{x}}(s)$, where s is the arc length. More generally, we will employ the hat, $\hat{\cdot}$, to denote the parametrization of any quantity along the fibre in terms of arc length. The time it takes the signal to propagate across the infinitesimal distance between two points $\hat{\mathbf{x}}(s)$ and $\hat{\mathbf{x}}(s)+\mathrm{d}\hat{\mathbf{x}}(s)$ is

$$\mathrm{d}T=\frac{|\mathrm{d}\hat{\mathbf{x}}(s)|}{c[\hat{\mathbf{x}}(s)]}, \tag{1}$$

with the potentially position-dependent speed of light $c[\hat{\mathbf{x}}(s)]$. In terms of the unit tangent vector $\hat{\mathbf{e}}(s)$, the vectorical increment $\mathrm{d}\hat{\mathbf{x}}(s)$ can be related to the scalar arc length increment $\mathrm{d}s$ via $\hat{\mathbf{e}}(s)\,\mathrm{d}s=\mathrm{d}\hat{\mathbf{x}}(s)$. This allows us to express the traveltime from the emitter to the scatterer and back in the form of the integral

$$T(L)=2\int_{s=0}^{L}c^{-1}\,\mathrm{d}s, \tag{2}$$

where we omitted the dependence of c on position for notational convenience. Assuming that the speed of light is constant, eq. (2) yields $T=2L/c$, which establishes a relation between the time when a back-scattered pulse is recorded and the distance L of the scatterer along the fibre. To produce spatially distributed measurements that only depend on fibre properties within a certain fibre segment, we consider another scatterer at distance $L+\Delta L$. The distance ΔL is the gauge length of the fibre-optic measurement system. It plays the role of an averaging length, and it affects the instrument response, as we will discuss later. The two-way traveltime for this scatterer is $T(L+\Delta L)=2\int_{s=0}^{L+\Delta L}c^{-1}\,\mathrm{d}s$, which yields the differential traveltime $\tau(L)$ of reflected pulses from the two scatterers,

$$\tau(L)=T(L+\Delta L)-T(L)=2\int_{s=L}^{L+\Delta L}c^{-1}\,\mathrm{d}s\,. \tag{3}$$

In the process of deformation, the material point at position $\hat{\mathbf{x}}$ moves to $\hat{\mathbf{x}}+\mathbf{u}(\hat{\mathbf{x}},t)$, where $\mathbf{u}(\hat{\mathbf{x}},t)$ denotes the space- and time-dependent displacement field. The neighbouring point moves from $\hat{\mathbf{x}}+\mathrm{d}\hat{\mathbf{x}}$ to $\hat{\mathbf{x}}+\mathrm{d}\hat{\mathbf{x}}+\mathbf{u}(\hat{\mathbf{x}}+\mathrm{d}\hat{\mathbf{x}},t)$, as illustrated in Fig.1 It follows that the original length of the infinitesimal segment changes from $|\mathrm{d}\hat{\mathbf{x}}|$ to $|\mathrm{d}\hat{\mathbf{x}}+\mathbf{u}(\hat{\mathbf{x}}+\mathrm{d}\hat{\mathbf{x}},t)-\mathbf{u}(\hat{\mathbf{x}},t)|$. In terms of the deformation tensor $\mathbf{F}$, with components $F_{ij}=\partial u_i/\partial x_j$, the new length can alternatively be expressed as $|\mathrm{d}\hat{\mathbf{x}}+\mathbf{F}(\hat{\mathbf{x}},t)\,\mathrm{d}\hat{\mathbf{x}}|$ or $|[\mathbf{I}+\mathbf{F}(\hat{\mathbf{x}},t)]\hat{\mathbf{e}}|\,\mathrm{d}s$. In addition to the change in length of a fibre segment, also its speed of light changes due to the photoelastic effect (e.g. Bertholds & Dändliker 1988) from the reference $c(\hat{\mathbf{x}})$ to $c[\hat{\mathbf{x}},\mathbf{F}(\hat{\mathbf{x}},t)]$. Following the same steps as for the reference state, we find an expression for the differential traveltime of the optical signal in the deformed fibre,

$$\tau(L)=2\int_{s=L}^{L+\Delta L}c^{-1}(\mathbf{F})\,|[\mathbf{I}+\mathbf{F}]\hat{\mathbf{e}}|\,\mathrm{d}s\,. \tag{4}$$

Eq. (4) relates the measurable differential traveltime to deformation of the fibre within the distance interval $[L, L+\Delta L]$. The above development is approximation-free, and it accounts for variations in the speed of light along the fibre and the photoelastic effect. However, it excludes the dependence of the refractive index on polarization and temperature (e.g. Nye 1957), as well as imperfections caused by limitations of the opto-electronics used to actually make the measurements in practice and the hardware needed to process, transmit and store the data. Hence, eq. (4) represents the exact and ideal instrument response of a distributed deformation sensor based on phase changes of backscattered light.

2.3 First-order approximations and the linearized relation to strain

While being exact, eq. (4) is impractical because the relation between the measured optical quantity and the deformation that we are interested in is nonlinear. Fortunately, when deformation is small, eq. (4) can be simplified. To obtain a useful first-order relation, we note that

$$\begin{aligned}|[\mathbf{I}+\mathbf{F}]\,\hat{\mathbf{e}}|^2=\hat{\mathbf{e}}^T(\mathbf{F}^T+\mathbf{I}^T)(\mathbf{F}+\mathbf{I})\hat{\mathbf{e}}=\hat{\mathbf{e}}^T\mathbf{F}^T\mathbf{F}\hat{\mathbf{e}}+\hat{\mathbf{e}}^T\mathbf{F}^T\hat{\mathbf{e}}\\+\hat{\mathbf{e}}^T\mathbf{F}\hat{\mathbf{e}}+\hat{\mathbf{e}}^T\hat{\mathbf{e}}\,.\end{aligned} \tag{5}$$

Omitting quadratic terms in deformation and using $\mathbf{e}^T\mathbf{e}=1$, we obtain

$$|[\mathbf{I}+\mathbf{F}]\,\hat{\mathbf{e}}|^2\doteq 1+2\hat{\mathbf{e}}^T\mathbf{E}\hat{\mathbf{e}}, \tag{6}$$

with the strain tensor $\mathbf{E} = (\mathbf{F}^T + \mathbf{F})/2$ and $\doteq$ meaning correct to first order. Denoting the axial strain along the fibre by $\varepsilon = \hat{\mathbf{e}}^T \mathbf{E} \hat{\mathbf{e}}$ and using the first-order Taylor expansion $\sqrt{1+2\varepsilon} \doteq 1 + \varepsilon$, we arrive at

$$\tau(L) \doteq \frac{2}{c_0} \int_{s=L}^{L+\Delta L} n(\mathbf{F})\,(1+\varepsilon)\,\mathrm{d}s, \tag{7}$$

where we expressed the speed of light in the fibre, c, in terms of its refractive index $n = c_0/c$ and the speed of light in vacuum c_0. The dependence of n on fibre deformation is experimentally known to take the form $n(\varepsilon) = n_0 + n_1\varepsilon$, with the opto-elastic coefficient $n_1 \approx 0.3$ (Bertholds & Dändliker 1988). Expanding the integrand, omitting quadratic terms and assuming that the refractive index is nearly constant within the gauge length, finally yields the differential traveltime for a backscattered signal recorded at time t,

$$\tau(L,t) \doteq \frac{2n_0}{c_0}\Delta L + \frac{2n_e}{c_0} \int_{s=L}^{L+\Delta L} \varepsilon(t)\,\mathrm{d}s, \tag{8}$$

with the effective refractive index $n_e = n_0 + n_1$. The first term on the right-hand side of (8) is the time-independent differential traveltime over the gauge length ΔL in the reference state. The second term is the differential traveltime change induced by deformation, which can be measured by means of optical interferometry in a DAS unit. To obtain measurements that are independent of some arbitrary reference state, DAS units measure differences of $\tau(L,t)$ over time. Subtracting measurements at times t and t_0, gives

$$\Delta\tau(L,t) = \tau(L,t) - \tau(L,t_0) \doteq \frac{2n_e}{c_0} \int_{s=L}^{L+\Delta L} [\varepsilon(t) - \varepsilon(t_0)]\,\mathrm{d}s\,. \tag{9}$$

Two special cases of eq. (9) are of practical interest. In the first one, t_0 serves as reference time when the fibre is defined to be in the reference state with $\varepsilon(t_0) = 0$. We then obtain

$$\Delta\tau(L,t) = \frac{2n_e}{c_0} \int_{s=L}^{L+\Delta L} \varepsilon(t)\,\mathrm{d}s\,. \tag{10}$$

Hence, the system measures strain. In the second special case, differential traveltimes of subsequent laser pulses are compared. When the timescale of deformation is large relative to the pulse rate—typically in the kHz range—the finite difference in (9) becomes a close approximation of a time derivative, and we can write

$$\dot{\tau}(L) \doteq \frac{2n_e}{c_0} \int_{s=L}^{L+\Delta L} \dot{\varepsilon}\,\mathrm{d}s\,. \tag{11}$$

Eqs (10) and (11) are first-order idealized instrument responses for strain and strain rate that assume small deformation. Although they are typically taken for granted, their validity deserves some discussion when deformation is large, for example, near seismic sources.

2.4 Examples of azimuthal and frequency response

The axial strain $\varepsilon = \hat{\mathbf{e}}^T \mathbf{E} \hat{\mathbf{e}}$, measured by DAS, is a projection of the full strain tensor $\mathbf{E}$ onto the direction of the fibre $\hat{\mathbf{e}}$. This projection induces a directional dependence of measurement sensitivity, meaning that the strength of a recorded signal depends on the angle φ between the fibre and the incoming wave vector. When the strain $\mathbf{E}$ is caused by a plane P wave, this angular dependence is proportional to $\cos^2\varphi$, and for a plane SH wave it is proportional to $\sin\varphi\,\cos\varphi$ (e.g. Benioff 1935; Lindsey & Martin 2021). Both are visualized in Fig. 2.

A more complete picture of the ideal DAS response for incident plane waves is shown in Fig. 3, which visualizes the amplitude spectrum of the optical traveltime change $\dot{\tau}(L)$ from eq. (4) as a function of the incoming wave azimuth of 100 Hz monochromatic P and horizontally polarized S waves measured by a straight fibre segment oriented in x-direction. In the reference case, where deformation is small and the wavelength is larger than the gauge length, the theoretical DAS spectrum is nearly identical to the spectrum of the incoming waves, as indicated by eq. (11). For P waves, nodal lines appear when the incidence angle is perpendicular to the fibre, that is, at 90° and 270°. S waves produce four nodal lines, at 0°, 90°, 180° and 270°.

Departures from the reference case occur for large deformation and high frequencies (or large gauge lengths). When deformation is large, for example in the vicinity of an explosive source, the linear approximation of eq. (11) becomes less accurate. As a consequences the DAS spectrum differs slightly from the spectrum of the incoming waves by a frequency multiple at 200 Hz, as shown in Fig. 3(b). For gauge lengths that are larger than the wavelength, either because the frequency is high or the gauge length is large, additional nodal lines appear for azimuths where a wavelength fits exactly into the gauge length. This effect is illustrated in Fig. 3(c). In such case the DAS measurement cannot be interpreted directly as strain (rate), and the gauge length effect must be accounted for explicitly in the data analysis and the forward modelling.

2.5 Ideal versus real DAS recordings

The instrument responses shown in Figs 2 and 3 are idealizations for plane waves that do not exist in such pure form in nature (e.g. Agnew & Wyatt 2014). Furthermore, the ideal responses are difficult to approach in practice because they omit numerous complications and details of the measurement technology.

Since the absolute phase of an individual laser pulse is random and cannot be measured directly, DAS interrogators employ interferometric techniques to recover relative phase changes. A portion of the laser output is split off to serve as a local oscillator, which is interfered with the Rayleigh backscattered signal. The resulting photocurrent contains an interference term that depends on the phase difference between the two fields, allowing strain-induced phase shifts to be measured. This principle also imposes a limit on the maximum measurable strain rate: if the phase change between successive measurements exceeds π, phase unwrapping can fail, leading to cycle skipping and an incorrect reconstruction of the strain signal. It follows that DAS measurements may become meaningless even before nonlinear effects in the instrument response become relevant.

Our derivations in Sections 2.2 and 2.3 were based on a gauge length defined exactly between some distances L and $L + \Delta L$ along the fibre. This corresponds to a boxcar window over which strain is averaged. DAS interrogators may implement the strain averaging slightly differently, with other window functions that the user may be able to choose. Consequently, the interpretation of the DAS output in terms of average strain may deviate from eqs (4) and (11).

An unavoidable complication is the presence of instrumental noise that may mask the signals of interest. Under laboratory conditions, noise floors as low as 1 picostrain/$\sqrt{\text{Hz}}$ have been reported

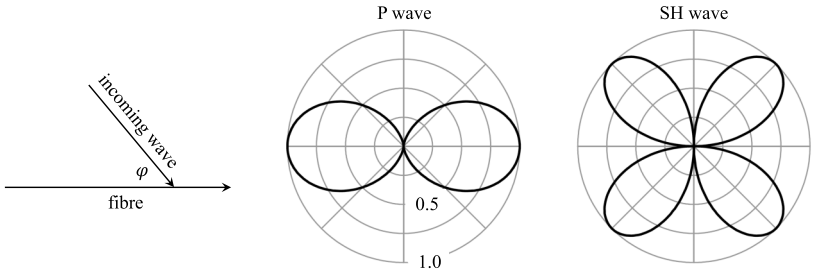

Figure 2. Angular dependence of DAS sensitivity. For an incoming *P* wave, measurement sensitivity is proportional to $\cos^2\varphi$, meaning that maxima appear when the wave travels parallel to the fibre. In contrast, measurement sensitivity for *SH* waves is proportional to $\sin\varphi\,\cos\varphi$, which produces two maximum sensitivity lobes at angles of 45° and 135°.

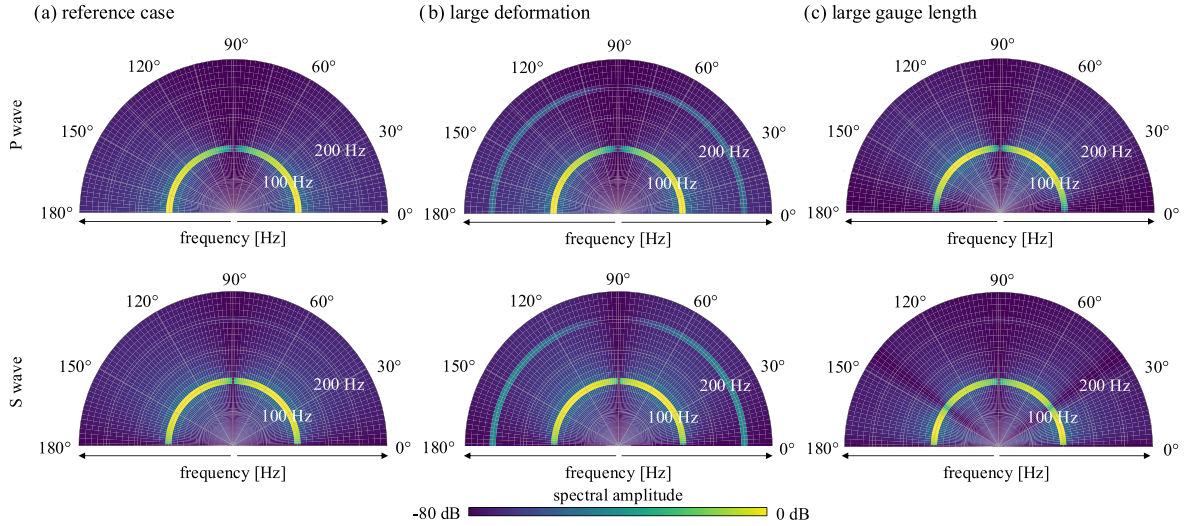

Figure 3. Theoretical amplitude spectrum of a DAS recording as a function of the incoming wave azimuth for a 100 Hz monochromatic *P* wave (top) and *S* wave (bottom). The fibre is straight and oriented in x-direction, as illustrated in Fig.2 *P* and *S* wave speeds are set to 5000 and 3000 m s^{-1}, respectively. (a) In the reference case, the gauge length is set to ΔL=10 m and the maximum strain amplitude to 10^{-6}. (b) For larger strain amplitudes of 10^{-4}, nonlinear effects appear in the form of a frequency multiple at 200 Hz. (c) For a large gauge length of ΔL= 50 m, additional azimuthal nodes appear because (apparent) wavelengths that fit within a gauge length are averaged out.

(e.g. Waagaard *et al.* 2021). In field experiments, however, such values can currently not be reached because the DAS unit is exposed to both mechanical and electromagnetic noise produced by the surrounding environment and human activity. In the collection of experiments described in Section 4, the smallest trustworthy signals had amplitudes on the order of 10 nanostrain s^{-1}.

In addition to mechanical deformation of the surrounding medium, temperature variations can also induce optical phase changes via thermal expansion and changes in refractive index, known as the thermo-optic effect. For optical fibres, the thermo-optic effect is about ten times stronger than the contribution of thermal expansion, and it leads to a temperature sensitivity on the order of 10 microstrain °C^{-1} (e.g. Sidenko *et al.* 2022). In seismological applications, the thermal effect can be significant when temperature changes quickly over timescales that overlap with the period band of the mechanical deformation signal.

At the level of the transmitting fibre, deformation-induced birefringence and intensity losses may affect the optical measurements. Their accuracy suffers due to the presence of electronic noise, limited stability of the laser and other opto-electronic component imperfections (Lapins *et al.* 2024). The bandwidth of the signals is limited by the hardware used to process, transmit and store the data. Cycle skipping issues when measuring phase changes may become important before nonlinearity does. Finally, the deformation of the medium of interest may only partly be transmitted into the fibre due to imperfect mechanical coupling.

Despite these complexities, DAS with well-coupled fibre-optic cables can achieve a nearly flat instrument response over a large frequency range from mHz to kHz (Paitz *et al.* 2021), thereby covering most environmental signals. When reliable strain amplitudes are important, the DAS data should be calibrated using conventional seismometers or other independent measurements. These conversions involve transformations between strain or strain rate and displacement or acceleration, for which numerous strategies have been developed. Details may be found, for instance, in Paitz *et al.* (2021) or Chien *et al.* (2025).

3 FIELDWORK DOS AND DON'TS

Although the ideal instrument response cannot be achieved in practice, DAS data acquired in icy environments can have exceptional quality, which is one of the reasons why cryosphere research is

among the most obvious niches for fibre-optic seismology. Compared to DAS experiments in cities or under water, cable geometry is often less constrained and can be optimized more easily. Covering the cable with snow is often sufficient to provide good coupling, and the amplitude of anthropogenic noise is typically low. Nevertheless, fibre-optic sensing experiments in the cryosphere are challenging due to remoteness and harsh climatic conditions. In the following sections, we provide practical fieldwork recommendations, concerning the choice and handling of fibre-optic cables, required equipment, data volumes and storage, splicing at low temperatures, timing of active experiments, cable layout and trenching, tap testing, and cable deployment and coupling in boreholes.

3.1 General

3.1.1 Choosing and handling suitable fibre-optic cables

In theory, most DAS units function with both single-mode and multimode fibres. However, it is still important to conduct test experiments to check that the modality of the fibre is indeed appropriate for the specific application and interrogator used. The effect of choosing loose-tube versus tight-buffered cable constructions is, however, small compared to the effect of cable coupling to the surrounding medium.

Different DAS unit manufacturers have different requirements for the condition of the cable at its furthest end. For an unterminated cable, large reflections can cause signal saturation in the section of the fibre furthest from the interrogator, meaning that its full length cannot be faithfully sampled. While some interrogator designs can compensate for such effects, others require that the fibre be optically terminated with an attenuator or that a section of redundant fibre is included beyond the main fibre under test to accommodate the signal saturation. A simple practical alternative that does not require splicing in the field is to introduce a series of tight turns at the end of the fibre that cause additional light loss and hence reduce the amplitude of reflections from the fibre end.

A launch cable can usefully be included between the interrogator and the fibre under test. The launch cable, typically 500–1000 m in length and wound in a tight spool, is not used for recording ground strains but allows losses at the input connector to the fibre under test to be quantified. The signal loss at the connection to the test fibre also accurately marks the beginning of the cable, thus providing support for a tap-test, covered in detail in Section 3.1.6. In making the first few hundred metres of the cable length redundant, the launch cable also removes the vulnerability to synchronization problems between the time of pulse emission and its first reception in the near-interrogator section of the cable. If the end of the fibre under test is unterminated, redundant cable may be attached to its end, again to accurately record its length without signal saturation from reflections at the termination.

Fibre-optic cables have a minimum bend radius that is typically on the order of a few centimetres. If the cable is bent around a tighter radius than this, it may be damaged. This is a key consideration when the cable is to be installed, for example, in a sequence of boreholes, where a single cable travels down the borehole, turns at its base and then returns to the surface. Consideration must be given to a reinforced assembly that prevents the turn in the cable from being tighter than the minimum bend radius. An alternative solution is to use fibre with a pre-installed bend at the end that links the down and return lengths of the fibre.

Fibre-optic cables tend to become significantly stiffer at low temperatures (e.g. Singh *et al.* 2023), meaning that they break more easily under any type of deformation. The reduced mechanical robustness, which is hard to quantify and depends on the degree of armour, must be taken into account especially during deployment and retrieval, and when the cable stretches under its own weight inside a borehole. Retrieving the cable intact is typically more challenging than deployment because stronger forces are required.

The weight of a fibre-optic cable is important also in the context of experimental logistics. Typical cables without metal tubes that can be used for deformation sensing, weigh around 10–20 kg km^{-1}. Taking into account that a cable drum has a weight of $\sim$10 kg, a few kilometres of cable may be carried by hand by two people. In addition to limiting the maximum length of the cable, the weight constraint also influences considerations on the mechanical stability of the cable. More stable cables are often heavier because they may include additional reinforcements such as metal tubes surrounding the fibre. In case a cable of the required length and stability does not fit onto a single cable drum, it must be distributed over several drums, and splicing in the field becomes necessary (see Section 3.1.4).

3.1.2 DAS interrogators and other equipment

As with any kind of field equipment, redundancy and robustness are critical, not only for the main measurement unit but also for peripherals, such as monitors and keyboards. For DAS experiments in the cryosphere, some additional aspects need to be taken into account. Historically, DAS units have been designed as rack-mounted systems for use in controlled environments such as field offices. However, cryosphere studies tend to be remote and field-based, often without infrastructure. By definition, the experimental conditions are challenging, and consideration must be made for environmental factors such as the working temperature range and blowing snow, for example. However, even without ruggedized DAS instruments, simple mitigation measures such as a tent for shelter, thermal insulation and ventilation have resulted in successful cryosphere applications. There is a significant difference between actively and passively cooled DAS systems. Actively cooled systems are more able to deal with confined environments, whereas passively cooled systems lack fans and rely on natural convection, limiting their thermal performance in tight spaces. In our experience, temperatures as low as $-20\,^{\circ}$C do not compromise the functioning of DAS units. In contrast, too much insulation may lead to overheating even of actively cooled interrogators, which can result in an automatic shut-down or even damage of the unit.

Most DAS instruments are designed to run with mains power, but the remoteness of cryosphere studies tends to preclude this. The power requirements of modern DAS units are continuously decreasing, but a typical power consumption is still at the level of 100s of Watts. The power consumption of additional equipment, including monitors and telecommunication devices, must not be forgotten. Hence, the use of inverters with batteries and solar panels, widely employed for other types of instruments, is still unrealistic for most DAS experiments. Portable petrol or diesel power generators are therefore currently the most convenient power source.

Considerations must be made for unintended shut-downs, refuelling and vibrations from this form of power supply. To protect the DAS unit, it should be connected to the generator via an Uninterruptible Power Supply (UPS), especially during longer experiments. The seismo-acoustic wavefield excited by power generators may

Figure 4. Optical fibre splicing in practice. (a) Splicing workplace set up in a tent near the EastGRIP camp site on the Northeast Greenland Ice Stream. Ideally, splicing should be done by a team of two in an environment that allows for focused work for potentially several hours. (b) An improvised workplace setup on a sled and a cable drum at several kilometres distance from the EastGRIP camp. (c) Schematic drawing of a splice box. An important feature that not all commercially available boxes have are the cable clamps that offer some tensile strength, which is important in the field.

significantly pollute DAS data recorded at several hundred metres distance, which needs to be accounted for in the design of the cable layout. Ideally, the interrogator and generator should be isolated from the field site, for example by deploying the interrogator and generator off the ice for a glacier deployment.

Natural and human-made seismic waves in cryospheric applications may have frequencies exceeding 100 Hz (see Section 4). S waves propagating through ice with a wave speed of $\sim$1800 m s^{-1} have wavelengths around 20 m or below. Near the surface of the firn layer, S wave speed may be as low as 200 m s^{-1} (e.g. Zhou *et al.* 2022; Fichtner *et al.* 2023b; Yang *et al.* 2024), resulting in seismic wavelengths at metre scale. It follows that typical seismic wavelengths are comparable to the gauge length of most DAS units. Depending on the manufacturer, the gauge length may be fixed and therefore specified at the procurement stage, or selectable as a parameter at the acquisition stage. The former must therefore be considered carefully to ensure the system meets the user requirements. The theoretical developments in Section 2.2 may help in making this choice.

3.1.3 *Data volumes and storage*

One of the most significant challenges presented by DAS is the large data volume. It can be computed as $V = N_c N_s V_s T$, where N_c is the number of channels, N_s the number of data samples per second, V_s the data volume in bytes occupied by one sample and T the total recording time in seconds. Assuming, for example, 10 000 channels (e.g. 1 m channel spacing along a cable of 10 km length), 1 kHz sampling rate, 4 bytes for a floating-point number and 1 month recording time, leads to V =104 TB. For comparison, the complete global-scale seismometer data archived by the Incorporated Research Institutions for Seismology (IRIS) from the early 1990s to 2020 occupy $\sim$700 TB (e.g. Arrowsmith *et al.* 2022).

3.1.4 *Splicing in the field at low temperatures*

Splicing is the tedious task of connecting two optical fibres such that light signals transmitted through the connection suffer only minimal intensity losses. Splicing in the field is necessary when cable segments on different drums need to be connected, a cable has been damaged or a faulty connector or termination needs to be replaced. Splicing is a challenge even in the lab. Producing high-quality splices on a glacier, under windy conditions and with freezing fingers is an art. Rehearsal sessions and patience are mandatory.

Considering that the production of a high-quality fusion splice may require hours of high-precision work, the working space should be set up in a tent with a camping chair and table, as shown in Fig. 4(a). Equipment should be placed in a weatherproof case. Owing to the notorious scarcity of electronics shops on glaciers and ice sheets, one of the main challenges of splicing in the cryosphere is to not forget any of the required equipment. In addition to the cleaver that produces a precise cut, and the splicer that fuses the two fibre ends together, numerous other utensils are needed. These include consumables like batteries for the splicer, pigtails (i.e. the right connectors), shrink tubes and patch cables in reasonably redundant quantities.

Most fusion splicers adjust the arc to compensate for atmospheric conditions during the splice. This means that there is a temperature range in which the splicer operates satisfactorily, typically between around -10 °C and 40 °C. Furthermore, there are limits on acceptable ambient pressure and humidity. While a fusion splicer from a specific manufacturer will work well in a laboratory environment, the results may be less optimal under harsh conditions.

Prior to splicing, essential safety measures should be taken, mostly to prevent fragments of optical fibres from causing apparently minor but potentially serious injuries. These measures include wearing safety glasses, nitrile gloves, closed shoes and long clothes. The latter two are obvious in the field, but must be considered in the lab. The DAS interrogator must be shut down before splicing to avoid damage of the unit and the eyes. A cable cutter and stripper are used to cut the cable to the desired length and isolate a single fibre. Utensils to clean the fibre include cleaning alcohol and lint-free wipes. As for many other tasks, duct tape is needed to fix already prepared fibres in a safe position. The spliced section of the cable is delicate and therefore a shrink tube (a plastic tube with a steel reinforcement rod) should be used to protect the splice. It is very easy, and very annoying, to forget to place the shrink tube over one of the cables ahead of splicing.

During splicing, it is recommended to wear a medical mask that helps to prevent the moist breath from causing microscopic water droplets at the tips of the cleaned fibres. Any waste, most importantly including any piece of fibre, should be carefully placed inside a sealable waste bag. Modern splicers typically feature a microscope, an automatic mechanism to align the two fibre ends and some quality checker that estimates the optical intensity loss across the splice. It is important to verify the quality of the splice with an Optical

Time-Domain Reflectometry (OTDR) device, which is usually integrated into the DAS unit.

After splicing, the shrink tube needs to be placed over the splice and heated. A useful splicer includes the required heating to minimize the amount of equipment. One of the artistic components of splicing is to ensure that the stripped fibre is not longer than the shrink tube. Subsequently, the splice should be placed inside a waterproof splice box, featuring cable glands and a mechanism to fix the cable, as illustrated in Fig. 4(c). Good alternatives to splice boxes are protective tubes, shown in Figs 4(a) and (b). Commercially available splice boxes may not be designed for cryospheric conditions and potentially require additional sealing, for example, with silicon gel. The splice box protects the fragile splice and partly restores the tensile strength of the fibre. Nevertheless, the splice box remains the most vulnerable part of the installation. While this vulnerability demands special care, it also comes with an important benefit: cables that are being strained by glacial flow will most likely break first at the well-defined position of the splice box, thereby ensuring that the rest of the cable remains intact.

3.1.5 Timing in active experiments

Most DAS units have a GPS-synchronized clock that provides accurate timing in continuous recording mode. When using DAS with an active source of seismic energy, consideration must be given to how to record source times. For active-source seismic surveys involving cabled geophones, this is often trivial because the recording can be initiated using, for example, a piezoelectric trigger switch on an impact source, a trigger geophone or a GPS-synchronized trigger. Since most DAS systems record active shots in passive continuous mode, recording cannot be triggered in the equivalent way. If active shots are being made along the cable length, then the source time may be approximated by noting where along the cable the first seismic energy is recorded, although the accuracy of this depends on the gauge length and possible near-source effects (Kennett *et al.* 2024). It can be possible to have the cable record a trigger signal: a fibre stretcher can be spliced into the length of cable under test, which can in turn introduce a diagnostic response into the cable when a signal generator receives a pulse from a piezoelectric tigger. However, the greatest flexibility likely comes when source times are recorded independently, using systems that are synchronized to GPS, such as a seismic event timer or dedicated passive geophone. Timing accuracy can be improved by using a higher sampling rate of the geophone adjacent to the source (Brisbourne *et al.* 2021).

3.1.6 DAS channel location and tap testing

Most seismological applications require precise knowledge about the geographic location where the data are recorded. DAS units only estimate the distance of a specific channel along the fibre, based on assumptions about its speed of light. Furthermore, the reference position, for example, metre zero, may not be known *a priori* because some fibre length is inside the DAS unit. Tap testing is the simplest and most common procedure to associate DAS channels with geographic location. When the cable is exposed at the surface, it can be tapped at a point for which the location is known, for example, from GPS measurements. In the case of buried cables, seismic waves can be excited near the cable, for example, by hammering or jumping. Typically, the geographic location is assigned to the channel where the signal arrives first or has the largest amplitude.

As a rule of thumb, the spacing of the tap tests should be on the order of 100 m, with denser spacing along more complex cable segments that contain bends or loops. In between the tap test positions, channel locations can be interpolated. Tap testing is most efficient when done with at least two people who communicate via radio. While one person performs the tapping, the other can inspect the data in real time and provide feedback on the visibility of the taps or the need to repeat the tapping at certain locations.

The accuracy of tap testing is inherently limited by the averaging over a gauge length that smears the signal in space. Furthermore, the first arrival or highest amplitude may not occur on the channel closest to the tap test because it is affected by the geometry of the cable, differences in coupling, subsurface structure, topography and other complexities (Kennett *et al.* 2024).

Tap testing is not possible in boreholes, but should still be done from the DAS unit to the point where the cable enters the borehole. This helps to account for the amount of fibre inside the DAS unit and provides a location reference at the borehole head. Inside the borehole, the cable stretches under its own weight. The magnitude of this effect can be estimated using information about the Young's modulus of the cable, which can usually be provided by the cable producer.

3.2 Surface experiments

Glaciers and ice sheets impose relatively few constraints on the fibre-optic cable geometry, thereby simplifying its optimization, for example, for seismic event detection and location. This flexibility is in contrast to densely populated or vegetated areas, and regions with rough terrain. The softness of ice compared to rock, or the presence of snow as insulating material, facilitate the coupling of the cable to the medium of interest, which often leads to remarkable data quality. Although these positive aspects turn the cryosphere into one of the most promising niches for fibre-optic surface experiments, there are practical challenges related to the cable layout and trenching.

3.2.1 Cable layout

Cable geometry primarily depends on the scientific questions one wishes to answer. Straight cables, for instance, facilitate 1-D f–k analysis, the extraction of surface wave dispersion and 2-D seismic imaging (e.g. Fichtner *et al.* 2023b; Yang *et al.* 2024). More complex geometries, for example, in the form of triangles or 2-D grids, are often more useful for event location (e.g. Walter *et al.* 2020; Hudson *et al.* 2021, 2025). For the optimal design of DAS cable geometries, methods similar to those used for seismometer arrays can be employed (e.g. Curtis 1999; Curtis & Maurer 2000; Rost & Thomas 2002; Maurer *et al.* 2017). However, adaptations are needed to account for the fact that neighbouring DAS channels along a cable cannot move freely in space and that there may be obstacles such a crevasse fields, landing strips or other no-go areas (Fichtner & Hofstede 2023).

In addition to the overall geometry of the cable, it is advantageous to include sections that are deployed in loops or zig-zags, as shown in Fig. 5, possibly with different orientations. Stacking over the channels in the loop suppresses noise and produces a high-quality directional antenna that may capture signals that are not visible on individual DAS channels. Also for noise reduction, the fibre should

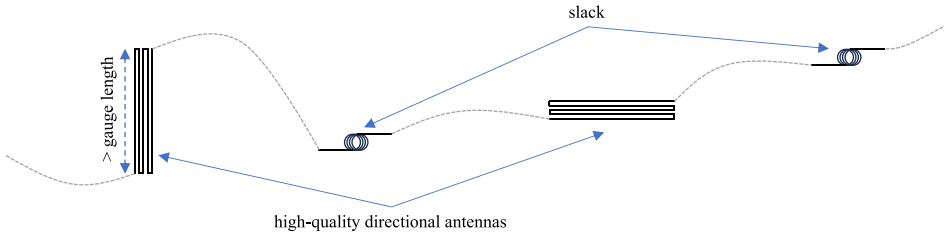

Figure 5. Schematic surface cable layout. The cable (grey dashed lines) includes looped sections (black solid lines) that serve as high-quality directional antennas or provide slack, especially needed on moving glaciers.

be looped back at the end of the cable to produce a duplicate of the data. Especially on fast-moving ice, smaller loops, schematically illustrated in Fig. 5, should be included to provide some slack and prevent snapping of the cable. When making turns, these should be done over at least a gauge length so that channels on both sides of the turn can be clearly isolated in the data. Key locations along the cable, including looped sections and turns, should be clearly marked with poles that remain visible after potentially heavy snow fall.

3.2.2 Trenching

To capture geophysical signals, the fibre-optic cable needs to be well-coupled to the medium below and protected from unwanted sources of deformation, such as wind or temperature variations. Covering the cable with few tens of centimetres of snow, if available, may already provide sufficient thermal insulation and coupling (e.g. Walter *et al.* 2020). If the cable can be deployed in autumn and kept in place until the first snowfall in winter, the work of covering the cable can be avoided (e.g. Klaasen *et al.* 2021; Hudson *et al.* 2025). Fig. 6 provides an example of the effect of snow cover on the amplitude of wind and acoustic noise recorded with a 9-km long cable deployed on Rhône Glacier in the Swiss Alps. Trenching the cable into the firn or ice generally provides better data quality, but it may be impossible to retrieve the cable intact unless there is sufficient snow melt in summer. In the presence of sufficient snow, a spade may be used to deploy the cable below the surface. Otherwise, manual trenching, for example, with a pickaxe, is typically unfeasible even over distances of few tens of metres, and some machinery is needed. Chain saws are effective over distances on the order of 100 m, but they come with a significant risk of injuries. Snow groomers or specially designed trenching sleds (Klaasen *et al.* 2022), as shown in Fig. 7, have proven useful.

Coupling a dark-coloured cable by letting it melt into the ice usually does not work. The melting process is too slow to reach a significant depth. In fact, cables covered by a thin snow layer rather tend to melt out.

3.2.3 Retrieval

A solution to retrieve the cable after the experiment for environmental reasons should be part of the field work planning. Trenching the cable deeper than around 0.5 m may make the retrieval more challenging than the deployment, and the risk of breaking the cable during retrieval increases. In warmer climates and in locations that are not too difficult to access, waiting for the next melt season should be considered as an option.

3.3 Borehole experiments

Borehole experiments come with additional technical challenges that are not a concern in surface deployments. They roughly fall into three categories: (i) the speed with which the cable can be deployed and retrieved, (ii) the mechanical stability of the cable and (iii) the mechanical coupling of the cable to the borehole wall. Furthermore, the presence of the borehole enables the propagation of guided waves, for example, Stoneley waves, which may interfere with the seismic phases of interest (e.g. Fichtner *et al.* 2023a).

The particular technical challenges do not pertain to all types of borehole deployments equally. The borehole length, borehole diameter, filling fluid and englacial temperatures dictate how cables have to be inserted and coupled to the ice walls. These parameters vary widely for drilling sites and purposes. The ice of temperate glaciers (e.g. most glaciers in the European Alps) is at the pressure melting point. In contrast, polar ice streams are at least partially cold and thus below the pressure melting point. This means that water flowing from the surface into the borehole can quickly freeze to its walls. In addition, cold ice is stiffer than temperate ice, which affects the deformation of boreholes under ice overburden pressure. A far-field approximation that ignores influences of valley sides as well as basal and surface topography, is given by parallel-sided ice slab flow with a parabolic deformation velocity profile u as a function of height above bedrock z (Paterson 1994),

$$u(z) = \frac{2A}{n+1}(\rho g \sin\alpha)^n \left[H^{(n+1)} - (H-z)^{(n+1)}\right], \tag{12}$$

where H is the ice thickness and α its surface slope (here 3°), g is gravitational acceleration (9.81 $\mathrm{m\,s^{-2}}$), ρ is the density of ice (~917 $\mathrm{kg\,m^{-3}}$), A is the flow law parameter (75.7 $\mathrm{a^{-1}MPa^{-3}}$ near the pressure melting point) and n is Glen's flow law exponent, typically taken as 3. After one year, the differential displacement between the surface and a depth of 10 m is only 40 cm, whereas the differential displacement between the bed and 100 m above it is over 145 m. This shows how boreholes can rapidly deform at greater depths, which may damage cables that are frozen to the ice walls. On the other hand, slight borehole inclination of a few degrees promotes coupling, as it can be sufficient to make the cable rest on the borehole wall and prevent it from hanging freely without mechanical connection to the ice (e.g. Fichtner *et al.* 2023a). However, this comes with the negative side effect of making the interpretation of seismic traveltime picks more involved than for a borehole that is practically vertical. In addition to longitudinal deformation, empty boreholes are subject to creep closure, and even the shallowest 100 m of a temperate borehole will close within a few years (eq. 27 in Talalay *et al.* 2014). This radial deformation and freeze-on by exchange of cold air during fall and winter seasons can lock the cable to the borehole walls and provide ideal coupling.

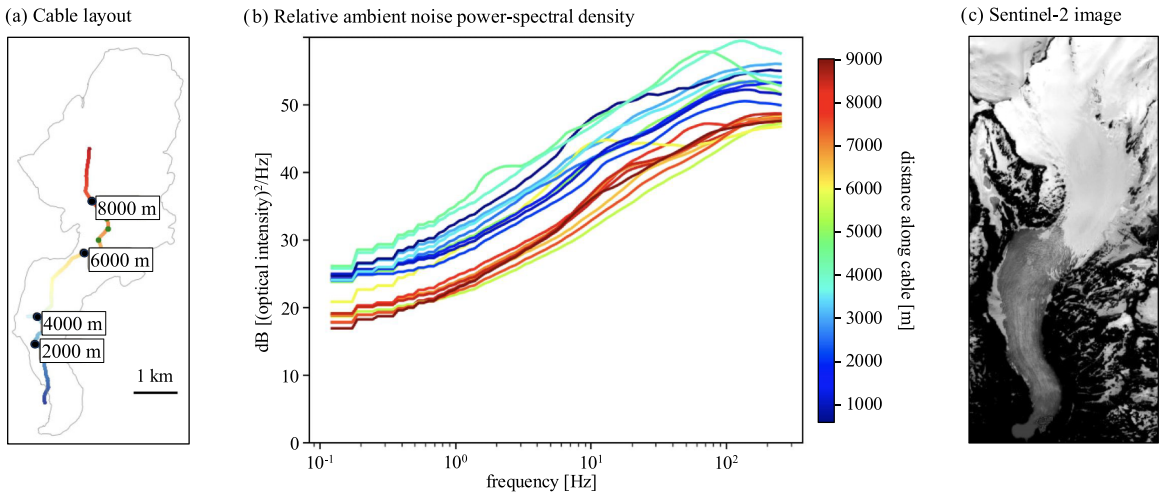

Figure 6. Effect of snow cover on ambient noise amplitude, mostly related to wind and acoustic waves. (a) Layout of the fibre-optic cable on Rhône Glacier, Swiss Alps. Colour coding corresponds to distance along the cable, and is the same as in panel (b), which shows the power-spectral density of the noise recordings as a function of frequency for different cable sections. Across all frequencies, the noise level decreases with increasing distance along the cable, that is, with increasing snow cover at higher altitudes. (c) Sentinel-2 image (visible and infrared wavelengths) of Rhône Glacier (Copernicus Europe's eyes on Earth).

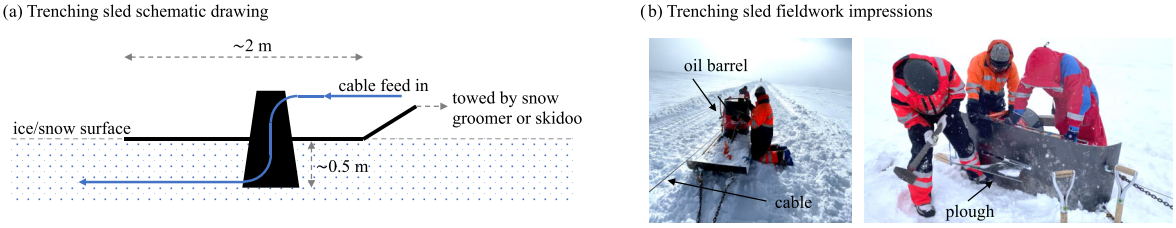

Figure 7. Trenching sled used to deploy a fibre-optic cable ~0.5 m under the surface. (a) Schematic drawing of the trenching sled, with the snow plough consisting of a ~2 cm thick steel plate and a metal pipe that guides the cable. The sled is towed by a snow groomer that also transports the cable drum. (b) Fieldwork pictures of the trenching sled from the Vatnajökull ice cap, Iceland (Klaasen *et al.* 2022). The filled oil barrel was used as an additional weight that prevented the sled from tipping over.

Although not guaranteed, we recently witnessed this situation on the Otemma Glacier in Switzerland.

For the purpose of borehole-deployed DAS, the drilling is usually done with the hot water technique, by which pressurized heated water is injected through a heavy drill bit, thereby melting a hole into the ice (Iken 1988). This technique is suitable for boreholes from a few tens to several hundreds of metres depth, although depths of up to 2500 m have been reached with specialized equipment (Benson *et al.* 2014). At the base, the borehole width may narrow to a few centimetres, depending on the drill bit design. The width grows towards the surface, where it typically measures ~30 cm in diameter or more. Boreholes drilled with the hot water technique tend to depart from perfectly vertical. Hence, within a few tens of metres below the surface, the cable touches the borehole wall. This enables frictional ice-cable coupling in addition to the coupling via the drilling water inside the borehole. When boreholes cross englacial or subglacial channels, their drilling water may drain, leaving friction or freeze-on as coupling mechanisms. Importantly, even glaciers and ice streams containing cold ice will likely have a temperate bed as a result of geothermal heat flux, basal friction and shear heating (e.g. Ryser *et al.* 2013). Hence, freeze-on at the ice sole is not guaranteed. Finally, it should be noted that even within temperate ice the cable can freeze onto the water-filled borehole walls around the water surface, because water pressure locally lowers the pressure melting point.

The nature of cable installations in coring boreholes may be different from hot-water drilled boreholes. Coring boreholes can be several kilometres deep and are drilled over several years, typically in locations with little expected borehole deformation. Coring boreholes have diameters of around 10–20 cm (e.g. Schwikowski *et al.* 2014; Fichtner *et al.* 2025) and are usually filled with a stabilizing viscous fluid (e.g. Sheldon *et al.* 2014) that can provide coupling between the ice and the cable (e.g. Brisbourne *et al.* 2021; Fichtner *et al.* 2023b). In such deep boreholes, the speed with which the cable is lowered into the borehole needs to be carefully controlled. The viscous drill fluid may prevent the cable from sinking with a reasonable speed. Since this effect is difficult to quantify *a priori*, one should be prepared to attach additional weights, on the order of a few kilograms, to the cable termination. Yet, a cable that sinks too quickly may become entangled inside the borehole. A sinking speed on the order of 10 cm s^{-1} seems to be a reasonable choice.

The mechanical stability of the cable is a major concern in borehole experiments. Most importantly, the cable's weight must not exceed its tensile strength, which may limit the maximum depth that can be reached. Although the tensile strength at room temperature is usually provided by the manufacturer, its dependence on temperature is typically not documented. The same holds, as discussed in Section 3.1.1, for the bending radius.

In addition to its own weight, the cable is subject to viscous drag from the drill fluid and friction from the borehole wall, both of

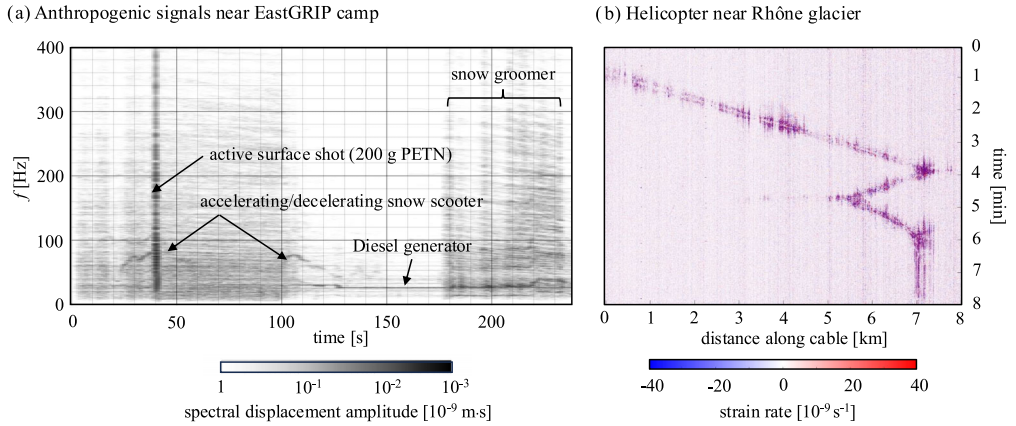

Figure 8. Collection of anthropogenic signals. (a) Displacement amplitude spectra of anthropogenic signals recorded within 5 min. near the camp of the East Greenland Ice Core Project (EastGRIP). (b) Strain rate recording caused by a helicopter flying near the Rhône Glacier in the Swiss Alps. The speed is around 180 km s^{-1}, and several sharp turns are clearly visible.

which are proportional to the lowering speed of the cable. Especially when the borehole wall is rough, scraping of the cable over the ice may damage its protective layers, thereby reducing its strength. The importance of this effect should be tested in smaller test runs, as it has already led to the loss of scientific instruments in deep boreholes. It follows that the maximum possible depth should be estimated conservatively, and the cable should be pulled up slowly.

4 CRYOSPHERIC SIGNAL GALLERY

The cryosphere is a rich source of signals from a wide range of natural processes, including surface crevassing, basal stick-slip icequakes, surface water flow, subglacial discharge, snow avalanches and many more. They often interfere with human-made signals that pollute the measurements or may even be misinterpreted as natural. In the following we provide a gallery of signals, intended to aid in future data analyses. To keep the presentation succinct, we limit ourselves to a description of the signals' main features, referring to earlier publications for more details. Some of the examples presented in the following paragraphs are included in the open-access data collection that complements this paper. More details can be found in the Appendix.

4.1 Human-made signals

Fig. 8(a) presents the amplitude spectra of human-made signals that are typically produced by fieldwork activities on glaciers and ice sheets. They have been recorded within only five minutes near the camp of the East Greenland Ice Core Project (EastGRIP) in July 2022 (Fichtner *et al.* 2025). The highest spectral power is from a surface explosion of 200 g PETN, with a bandwidth of several hundred Hz. In contrast, the engines of the diesel electricity generator and a snow scooter produce narrow spectral lines. The activities of a snow groomer, used to prepare the airplane landing strip, are visible in a frequency range from few Hz to several hundred Hz. Signals from air traffic are often easy to identify based on their apparent propagation speed, which is too low for seismic waves and too fast for ground traffic. The recording in Fig. 8(b) originates from a helicopter flying at ∼180 km hr^{-1} near Rhône Glacier in the Swiss Alps.

A space-time domain version of an active surface shot recording made by Booth *et al.* (2020) in a 1000 m deep borehole on Store Glacier, West-Central Greenland, is shown in Fig. 9 and contained in the open-access data collection. The borehole was drilled using pressurized hot water, and it drained rapidly on breakthrough by intersecting the basal interface. Subsequently, the cable froze into the borehole, thereby providing excellent coupling to the surrounding ice. The source consisted of repeated sledgehammer strikes on a polyethylene impact plate, around 30 of which were stacked to produce the data in Fig. 9 For a zero-offset source, the recordings are dominated by the direct *P* wave, with wave speeds slightly increasing from ∼3750 m s^{-1} near the surface to ∼4000 m s^{-1} in the lowermost 100 m. A Stoneley wave is visible in the upper ∼150 m. It interferes with *P* waves that were most likely scattered by surface crevasses. At larger offsets, vertically polarized *S* waves can be recorded by the fibre-optic cable.

4.2 Natural signals

4.2.1 Glacial seismicity

The deformation of glaciers and ice sheets involves processes that operate on timescales ranging from milliseconds to years. Viscous deformation in the form of long-term flow may not be measured easily with current fibre-optic sensing technologies for various reasons. These include the limited low-frequency response of most interrogators, the difficulty of coupling a cable sufficiently well for several weeks or months and the logistical challenges of running long-term fibre-optics experiments on glaciers. In contrast, short-term brittle deformation and the resulting seismic waves can often be recorded easily.

Fig. 10 shows examples of glacial seismicity observed on Rhône Glacier in the Swiss Alps, which are part of the open-access data collection. The experimental setup consisted of a triangular DAS array above ∼200 m thick ice (Walter *et al.* 2020). The stick-slip icequake in Fig. 10(b) occurred at the interface between ice and bedrock. It produced clearly visible *P* and *S* waves, as well as multiple reflections between that interface and the surface. Crevassing events that occur closer to the surface, such as the one in Fig. 10(c), are typically dominated by a dispersed surface wave train and less prominent body waves.

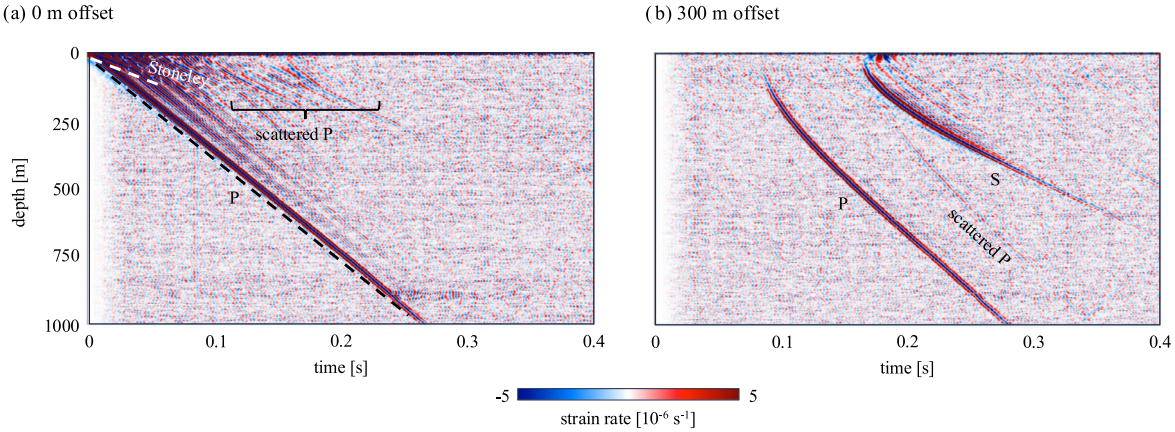

Figure 9. Borehole DAS data collected on Store Glacier, Central-West Greenland (Booth *et al.* 2020). (a) Zero-offset recording containing the direct *P* wave and a Stoneley wave. Later arrivals at shallow depth are interpreted as waves scattered from surface crevasses. (b) Recording for a source at 300 m distance from the borehole, dominated by the direct *P* and *S* wave arrivals. The scattered *P* wave was likely produced by a fracture near the shot location.

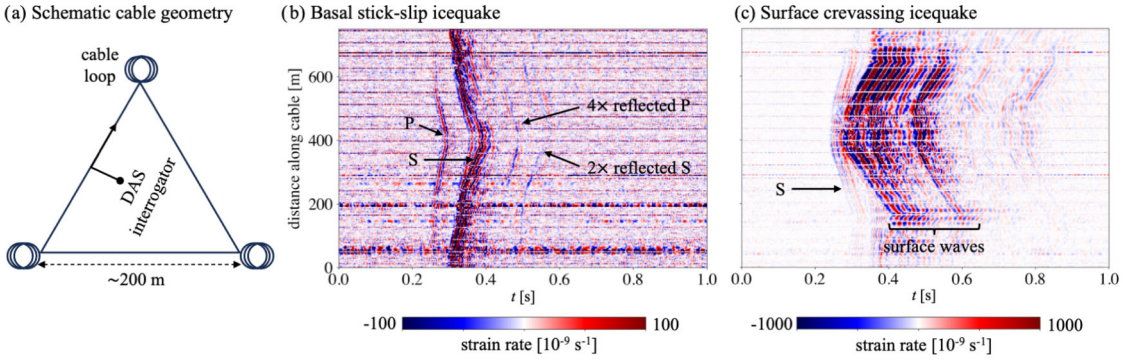

Figure 10. Examples of a basal stick-slip icequake and a surface crevassing icequake recorded on Rhône Glacier, Swiss Alps. (a) Schematic illustration of the triangular cable layout, including loops in each of the corners. Grey numbers are distance along the fibre. (b) Recording of a basal stick-slip icequake, including multiply reflected *P* and *S* waves. (c) Recording of a surface crevassing event, dominated by dispersed surface waves.

DAS arrays have also been deployed in the Antarctic. Fig. 11 shows an example of a basal stick-slip icequake from the ∼2 km thick Rutford Ice Stream sliding at ∼400 m yr^{-1} (Hudson *et al.* 2021) that is also part of the open-access data collection. In contrast to the Alpine glacier example in Fig. 10, this Antarctic ice stream has a ∼80 m firn layer, causing waves to be refracted vertically towards the surface. This effectively mutes the sensitivity of the fibre to *P* waves originating from depth, since the *P* waves become vertically polarized with the horizontal fibre only sensitive to horizontal strain. Therefore, only icequake *S* waves are observed, as illustrated in Fig. 11(b). Since the velocity structure of ice is simpler than rock, it is straightforward to perform full-waveform source inversion. Full-waveform source mechanism inversion results for the example icequake from DAS and geophones are shown in Figs 11(c) and (d), respectively. Even though the DAS fibre only covers a small portion of the focal sphere compared to the geophones, the uncertainty in slip vector is significantly reduced (∼45° compared to ∼270° for the geophones). This result is interpreted to be a combination of far more observations (1000 DAS channels versus 10 geophones), combined with focal mechanisms in strain-space being segmented into octants rather than quadrants in velocity-space. These results highlight the added value of DAS beyond conventional instrumentation for studying natural glacial seismicity.

In addition to basal stick-slip and surface crevassing icequakes, cascades of englacial icequakes have been observed with a 1.5 km long fibre-optic cable inside the EastGRIP borehole (Fichtner *et al.* 2025) in the upstream part of the Northeast Greenland Ice Stream. An example of an upward migrating cascade is visualized in Fig. 12 and included with additional examples in the open-access data collection. The depths where subevents occur are correlated with the depths where volcanism-related impurities, such as tephra particles and elevated SO_4 content, have been measured. Temporary unwelding of horizontal interfaces within the ice seems to prevent the upward transmission of the emitted seismic waves, thereby making these events unobservable at the surface. Near EastGRIP, this kind of englacial seismicity is likely to make a significant contribution to the overall deformation of the ice stream, but further experiments are needed to assess the global relevance of this phenomenon.

Ice shelves and other floating ice bodies can exhibit a wide range of wave propagation modes, resulting from the interaction of the ice with the underlying water and the atmosphere above. These include Crary waves (e.g. Ewing & Crary 1934; Press & Ewing 1951), buoyancy-driven gravity waves (e.g. Ewing & Crary 1934; Oliver *et al.* 1954), ocean wave-driven flexural waves (e.g. Cathles *et al.* 2021; Meylan *et al.* 2021), air-coupled flexural waves on lake or pack ice (e.g. Nziengui-Bâ *et al.* 2023; Xie *et al.* 2024) and many more. Fig. 13 shows an unusual example of flexural gravity

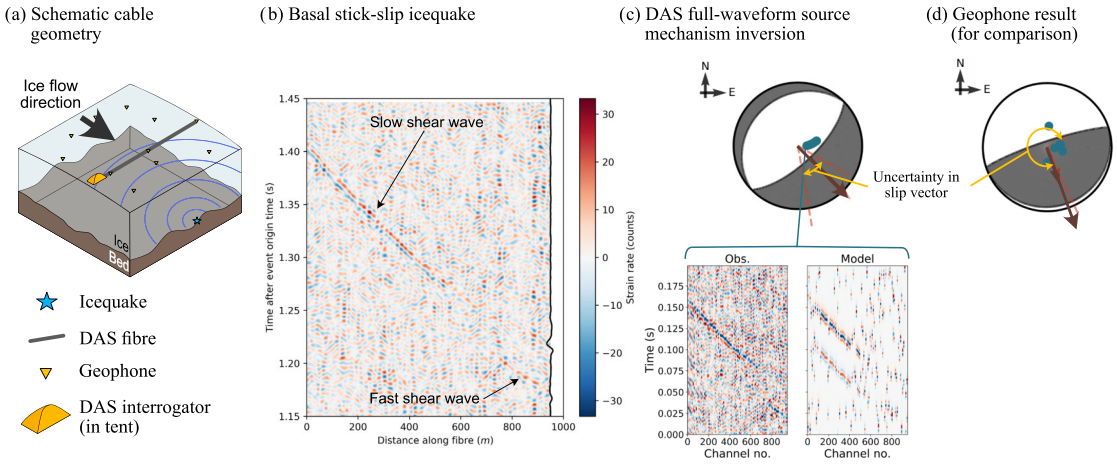

Figure 11. Example of a basal icequake from Rutford Ice Stream, Antarctica, modified from Hudson *et al.* (2021). (a) Schematic of the cable geometry (fibre was deployed perpendicular to ice flow). Ice flow is ∼ 160° from north. (b) DAS recording of a basal stick-slip icequake, with fast and slow shear waves caused by anisotropy. (c) DAS full-waveform probabilistic source mechanism inversion result. Red arrow shows slip vector and yellow arrows show uncertainty in slip vector. (d) Same as (c) but using geophones instead of DAS.

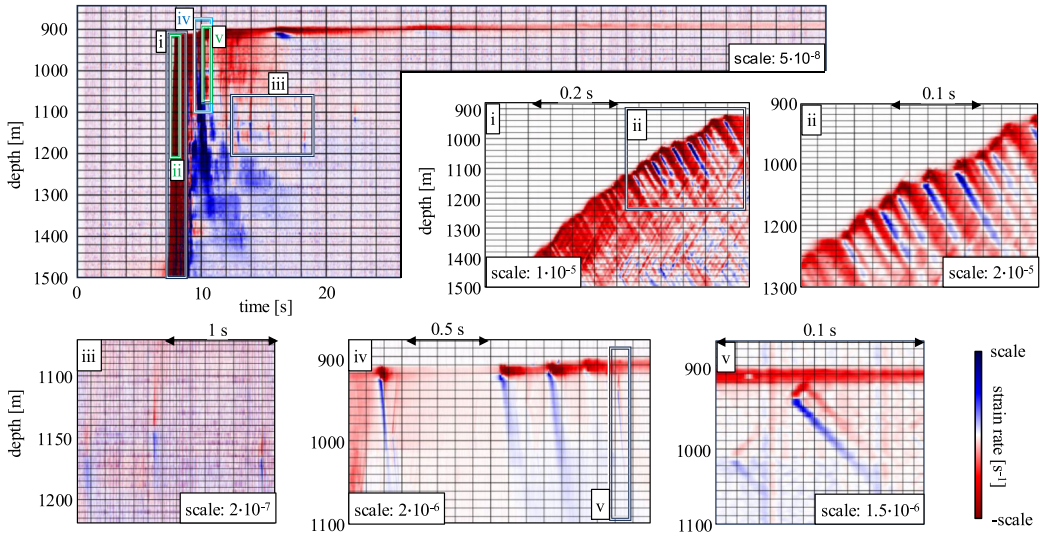

Figure 12. Example of englacial icequake cascades observed inside the EastGRIP borehole (Fichtner *et al.* 2025), with close-ups shown in panels (i)–(v). The event has distinct multiscale characteristics, including the main upward-propagating cascade of events in panels (i) and (ii), smaller individual events in panels (iii) and (iv), as well as long-lasting creep around 900 m depth and nearly perfect downward reflections in panel (v).

waves observed on a floating ice sheet atop the subglacial lake of Grímsvötn volcano in Iceland, which is covered by Europe's largest ice cap, Vatnajökull (Fichtner *et al.* 2022b). Low-magnitude volcanic tremor is the most likely source of the nearly monochromatic fundamental-mode eigenoscillation of the ∼300 m thick ice sheet. The deformation causes periodic extension and compression that results in strain rates on the order of 10^{-9} s^{-1} that can be clearly observed using a fibre-optic cable of several kilometres length, trenched at the surface of the ice.

4.2.2 Ice fabric

At fast-flowing glaciers and ice streams, ice crystals can reorient, enhancing viscous deformation compared to isotropic ice (e.g. Duval *et al.* 2010). Since ice crystals are anisotropic, this translates into seismic velocity anisotropy (e.g. Gajek *et al.* 2021; Kufner *et al.* 2023; Leung *et al.* 2025) and the splitting of shear waves into a fast and a slow component, polarized relative to the ice crystal orientation (e.g. Teanby *et al.* 2004; Hudson *et al.* 2023a). To observe shear wave splitting, 2-D horizontal wavefield sensitivity is required. This can be achieved with a 2-D DAS array geometry, such as a triangle, for example. A first attempt at inferring seismic anisotropy using DAS can be found in Hudson *et al.* (2021), with a summary of results shown in Fig.14 Here, a triangular cable array geometry is used, with amplitude ratios of the strain-rate across the three triangle edges compared to simulated values, to infer the likely orientation of the fast *S*-wave polarization. Results for the ice quake used are in close agreement with geophone-derived measurements from the same ice stream (Smith *et al.* 2017). One should note that this is a first attempt, with formal inversion schemes not yet developed for performing DAS shear-wave splitting inversion.

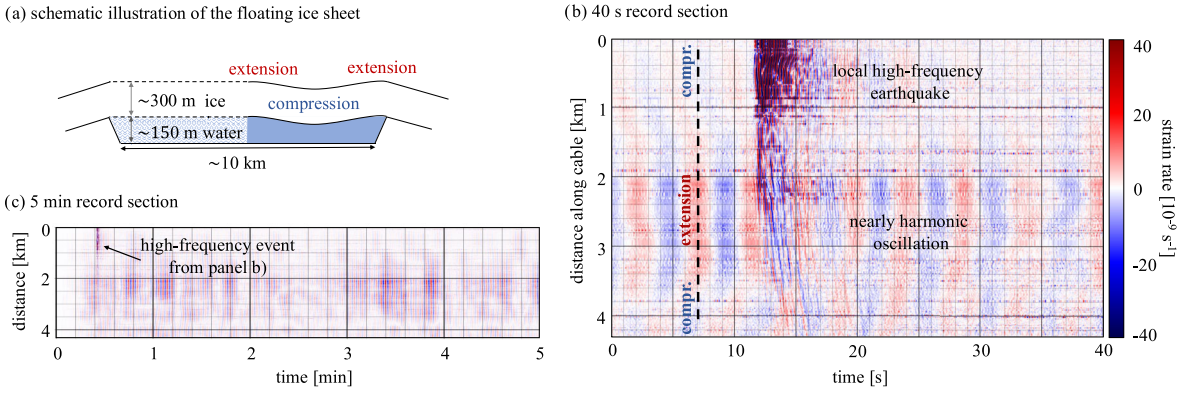

Figure 13. DAS observations of floating ice sheet resonance in the caldera of Grímsvötn volcano, Iceland. (a) Schematic geometry of the resonating system, consisting of the ∼300 m think ice sheet floating atop the subglacial lake. (b) Record section of 40 s length, containing a high-frequency volcanic earthquake superimposed on the nearly monochromatic ice sheet oscillation with a frequency of ∼0.22 Hz. (c) Record section of 5 min length, showing slight variations of the oscillation amplitude on minute timescales.

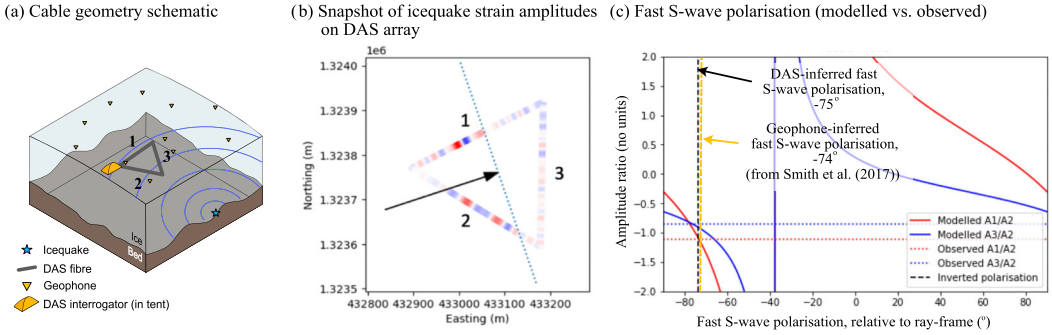

Figure 14. Ice fabric seismic anisotropy estimate from DAS observations at Rutford Ice Stream, Antarctica. Results from Hudson *et al.* (2021). (a) Cable geometry. (b) Example of instantaneous strain amplitudes along the fibre for an ice quake. (c) Modelled versus observed amplitude ratios across different sections of the triangular DAS array with varying fast *S*-wave direction. Dashed black line indicates optimal DAS result, with dashed yellow line indicating equivalent result from a geophone-derived measurement by Smith *et al.* (2017).

4.2.3 Glacier hydrology

Flowing water generates a rich seismo-acoustic wavefield through a variety of processes, including wave breaking, the formation of hydraulic jumps and the entrainment and collapse of air bubbles in turbulent flow. An example of a predominantly liquid water-induced soundscape recorded by DAS is shown in Fig. 15 for an experiment conducted on Rhône Glacier in the Swiss Alps. Owing to the, at that time, unpredictable sequence of Covid-19 lock-downs, the experiment was conducted in summer. In the absence of fresh snow, most of the 8 km long cable was exposed at the surface (see Fig. 6). Although this seemingly unfavourable setup largely precluded the recoding of glacial seismicity, it produced a densely sampled data set of quasi-random ambient noise originating from the flow of surface water, produced by both melting and precipitation. As expected, the noise amplitude is highest in the ablation zone, however, without showing an obvious correlation with temperature and precipitation. Nevertheless, Manos *et al.* (2024) were able to train a machine-learning model that predicts proglacial discharge, clearly outperforming standard models trained on meteorological data.

4.2.4 Snow avalanches

Existing telecommunication cables can be used to record deformation caused by snow avalanches. Fig. 16(a) shows example data that are included in the open-access data collection. They were recorded with a ∼700 m long cable used for communication with scientific instruments on the slope of the Swiss avalanche test site in the Vallée de la Sionne (Paitz *et al.* 2023). The top end of the cable is located at 1660 m above sea level and the bottom end, where the DAS unit was installed, is inside a bunker ∼200 m lower. Most avalanches, including the transitional snow avalanche shown here, propagate nearly parallel to the cable. The fast-moving front contains three individual surges and is followed by a slow-moving powder cloud. Deformation signals are generated by a combination of the seismo-acoustic near- and far-fields, and by quasi-static deformation.

Far-field seismic waves are the main constituent of the snow avalanche in Fig. 16(b), recorded with a telecommunication cable that follows the Fluelapass road in the Swiss Alps (Edme *et al.* 2023). The avalanche released on a slope next to the pass road, propagated downhill nearly perpendicular to the road, but did not reach the cable.

5 FRONTIERS AND CHALLENGES

Cryosphere research has emerged as one of the most attractive niches for fibre-optic sensing. In the following sections, we highlight outstanding scientific questions to which fibre-optic sensing could

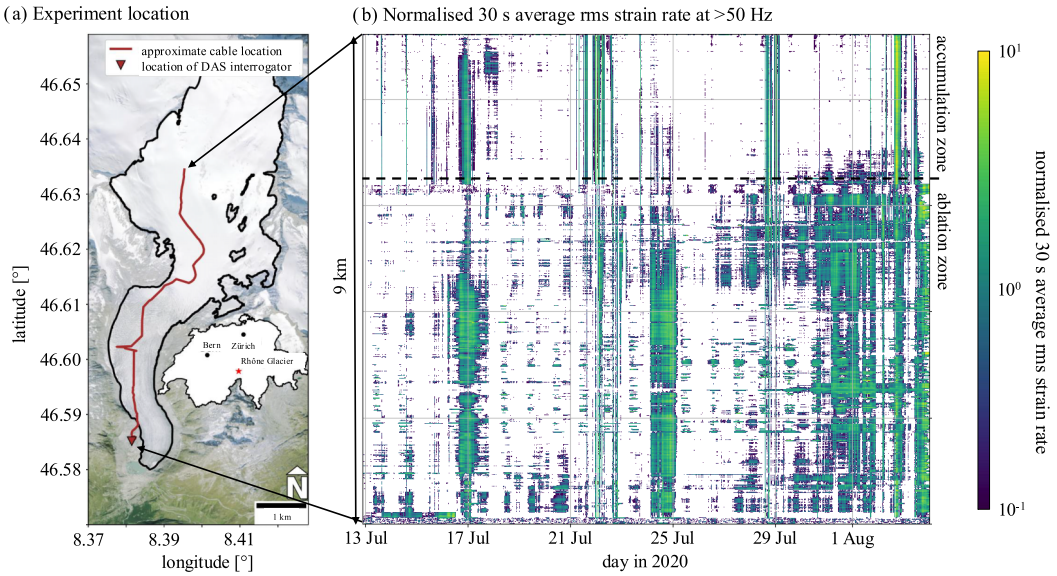

Figure 15. Seismo-acoustic wavefield dominated by surface water flow on Rhône Glacier in summer 2020 (Manos *et al.* 2024). (a) Location of the experiment, involving a 9 km long fibre-optic cable, largely exposed at the surface. (b) Normalized 30 s average of the rms strain rate, high-pass filtered at 50 Hz. The approximate transition from the accumulation zone to the ablation zone is marked by the dashed line.

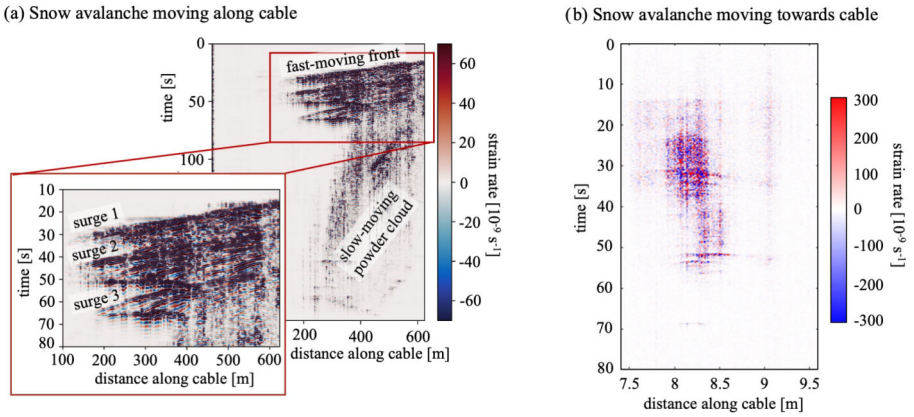

Figure 16. DAS recordings of snow avalanches. (a) Transitional snow avalanche propagating atop and approximately parallel to a fibre-optic cable at the Swiss avalanche test site in the Vallée de la Sionne (Paitz *et al.* 2023). (b) Snow avalanche propagating towards a telecommunication cable along the Fluelapass road in the Swiss Alps (Edme *et al.* 2023).

make significant contributions in the future, but also list technical challenges that remain to be overcome.

5.1 Science questions

Anthropogenic climate change is driving atmospheric and oceanic warming, which in turn is driving rapid change of the cryosphere. Looking forward, there are a number of outstanding challenges associated with understanding and monitoring the cryosphere in a warming world. Fibre-optic seismology is an ideal tool to provide enhanced understanding of the involved processes. A non-exhaustive list of related scientific challenges is as follows.

Ice dynamics models used to estimate sea-level rise projections still lack sufficient observational constraints on critical boundary conditions. While we can quantify fracture damage near the glacier surface (e.g. Chudley *et al.* 2019; Lai *et al.* 2020), observations and monitoring strategies of subsurface fracture damage remain sparse to non-existent (Oppenheimer *et al.* 2019). Subsurface observations are essential for verifying the importance of fracturing and marine ice cliff instability on sea-level rise projections (Pollard *et al.* 2015a). Similarly, quantifying ice-bed friction better is essential for reducing uncertainty in sea-level rise projections (Oppenheimer *et al.* 2019). Although recent work using surface dynamics to infer basal conditions has shown promise (Riel *et al.* 2021; Ockenden *et al.* 2022), direct seismic measurements of glacier bed conditions remain limited to scales of a few kilometres (e.g. Zoet *et al.* 2012; Brisbourne *et al.* 2017; Muto *et al.* 2019; Gräff & Walter 2021; Hudson *et al.* 2023b). Furthermore, interactions of ice with the ocean at marine-terminating glaciers play an important role in controlling continental ice loss (Weertman 1974; Joughin *et al.* 2012; Kochtitzky *et al.* 2022), yet these regions are generally poorly instrumented for practical reasons. DAS is a

promising technology for addressing these outstanding challenges. It can provide dense spatial and temporal sampling over tens to hundreds of kilometres, and it may be deployed in traditionally inaccessible terrain, for example, in crevasse fields (Hudson *et al.* 2025) or from coastlines into the open ocean (Peña Castro *et al.* 2023).

Fibre-optic sensing has the potential to overcome current challenges in monitoring long-term changes of the cryosphere. For example, permafrost has been shown to play an important role in storing greenhouse gases (Miner *et al.* 2022) and the stability of mountain slopes (Fey *et al.* 2025). Although seismology is an effective tool for monitoring permafrost changes (e.g. Lindner *et al.* 2021; Cheng *et al.* 2022; Lindner *et al.* 2025), scaling up observations based on conventional seismometers is difficult. A further challenge is monitoring the stability of Alpine land-terminating glacier fronts. These glacier fronts are becoming increasingly unstable with warming temperatures, posing a risk to Alpine communities (Faillettaz *et al.* 2015). Again, while seismology shows promise for monitoring Alpine glacier stability (Chmiel *et al.* 2023), deploying conventional instrumentation in such terrain continues to be a major problem. DAS by itself may not fill these data gaps, but the possibility to deploy cables in difficult terrain and keep them without maintenance for months or years, is likely to make a significant contribution in the future.

As a result of their accessibility, temperate glaciers have traditionally been the focus of *in situ* glaciological measurements, including some of the first DAS deployments (e.g. Walter *et al.* 2020; Manos *et al.* 2024; Hudson *et al.* 2025; Zitt *et al.* 2025). In these settings, summer months or changes between winter and summer seasons are of primary importance, since following the onset of surface melt production, the subglacial hydraulic system transitions from inefficient to efficient configurations (e.g. Werder *et al.* 2013). This transition leads to variations in basal sliding and overall ice flow result, which provides opportunities to investigate incompletely understood relations between subglacial processes and ice dynamics. In this context, the monitoring of basal seismicity is key to scientific progress. However, long-term seismic instrumentation on snow-free high-melt glacier surfaces is a challenge, because sensors have to remain levelled and protected from environmental disturbances. DAS could overcome this challenge. Fibre-optic cables can be rapidly deployed, require little or no maintenance and can densely cover an entire glacier (Manos *et al.* 2024), which is practically impossible with conventional seismic installations. Unfortunately, snow-free ice surfaces also imply high-noise DAS data (see Section 3.2.2). For glacier-wide monitoring, efficient ice trenching is therefore needed, to shield the cable even when several metres of ice melt within a few months (e.g. Huss *et al.* 2015). Alternatively, modern denoising algorithms could be tuned towards cryo-seismological DAS data and used to identify ice quake signals in the presence of noise resulting from poor cable-ice coupling and meteorological influence (Zitt *et al.* 2025).

Long-term DAS measurements could also offer other insights into glacier hydraulics. Monitoring basal reflections within ice quake signals (Walter *et al.* 2020) may detect hydraulic changes at the bed without the need for repeated active seismic sources (Nolan & Echelmeyer 1999). If high-frequency seismic signals from ice quakes or ambient seismic noise were available, characterization of the shallowest metres of the ice column would elucidate the weathering crust, which is an important intermediate water storage but still poorly researched (Cook *et al.* 2016).

Finally, the propagation of velocity variations along a glacier's flow line can serve as a diagnostic tool to understand basal sliding. These kinematic waves (Pfeffer 2007) explain the instability of Greenlandic tidewater glaciers (Felikson *et al.* 2017). On much slower flowing Alpine ice, their identification requires high-precision distributed measurements of surface deformation. While DAS can measure deformation in the tens of nano-strain range, GPS receivers, whose installation in glaciers requires frequent maintenance of antenna poles, have a location accuracy at the centimetre scale (e.g. Riesen *et al.* 2010). Quasi-static DAS measurements could therefore be well suited to track the propagation of kinematic waves and other velocity variations.

5.2 Experimental and technical challenges

A major conclusion of Section 5.1 is that long-term and long-distance cryospheric DAS experiments are both key to further scientific advances and an outstanding open challenge. The duration of DAS experiments on glaciers is limited by the flow of the ice, which eventually ruptures the cable. Ironically, data collection is most difficult in those parts of a glacier that may be most interesting. Deploying the cable in tubes, where it has some freedom to move, might be a solution, but it increases the logistical effort and likely decreases coupling. While cables of up to few kilometres length may be deployed manually, longer cables require a faster automated procedure. Purpose-built trenching sleds, like the one shown in Fig. 7, may be a solution, but they require a powerful towing vehicle to plough through the ice.

Long-distance experiments are further complicated by the limited range of DAS, typically several tens of kilometres, depending on fibre quality and noise conditions. Extending the maximum interrogation distance may require the adoption of alternative sensing concepts, based, for example, on phase and polarization measurements of transmitted laser signals (e.g. Marra *et al.* 2018; Mecozzi *et al.* 2021; Bogris *et al.* 2022). The use of transmitted instead of backscattered signals trades the high spatial resolution of DAS for a longer interrogation distance. However, some spatial resolution can be achieved by deploying cables not in straight lines but more complex geometric configurations (Fichtner *et al.* 2022a). Long-range phase- and polarization-based systems have so far only been tested on land and under water. Their usefulness for cryosphere research is still an open question.

Improving data coverage, for example, for imaging and source inversion, will not only require longer distances but also the simultaneous measurement along cables at the surface and in multiple boreholes. While such experiments are possible with today's technologies, their complexity, compared to the cryospheric experiments performed so far, poses logistical challenges.

An alternative approach to improve data coverage is the use of helically wound fibre cables (e.g. Kuvshinov 2015; Ning & Sava 2018). In contrast to cables containing straight fibres, helical winding removes the zero-sensitivity nodes in the angular DAS response, exemplified in Fig. 3 The benefit of helically wound fibre cables is that P and S waves can be recorded for all incidence angles. This comes at the cost of a higher weight of $\sim$500 kg km^{-1}, compared to 10–20 kg km^{-1} for standard cables without metal reinforcement. Whether benefit and cost are in a reasonable balance for cryospheric applications, is currently unclear.

The data volumes of future DAS experiments may grow more rapidly than currently available storage solutions, such as RAID or

cloud systems (Ni et al. 2025). Future DAS deployments of 2-D cable grids at the surface, combined surface-borehole experiments and the emergence of DAS units that can interrogate multiple fibres, are likely to be particularly challenging. Our current practice of trying to store all DAS data permanently is therefore unlikely to be sustainable. The priority may need to shift towards keeping only scientifically valuable data, although scientific value is hard to foresee. Conventional downsampling in space and time may be combined with compression algorithms that are specifically tuned towards DAS data and may operate in real time (e.g. Dong *et al.* 2022; Issah & Martin 2024; Segui *et al.* 2025). Furthermore, science may need to be done on-the-fly, for example, by deleting raw data after rapidly picking traveltimes, computing noise correlations or dispersion curves, or detecting and locating seismic events. Emerging machine-learning methods, adapted to specific research questions in cryo-seismology (e.g. Willis *et al.* 2025; Zitt *et al.* 2025) may enable or accelerate this mode of operation. While possibly being unavoidable, deleting raw data causes issues with the reproducibility of scientific results that need to be discussed in the community.

Looking more generally toward future developments in optical fibre sensing, we suggest that the geophysical research community consider issuing more open Requests for Information (RFIs) and Requests for Proposals (RFPs), designed to encourage innovation in system design by hardware manufacturers. To date, much of the community has adopted a pragmatic approach, working primarily with commercially available systems, without harnessing the creativity and expertise of optical engineers. Although RFIs and RFPs are sometimes viewed as burdensome due to the associated administrative processes and time requirements, they represent a powerful mechanism for articulating specific research needs and catalysing targeted development. Areas where we anticipate meaningful advancements include reductions in power consumption, improvements in sensing aperture, enhancements in dynamic range and the ability to measure absolute strain. While measurements of absolute strain integrated over a fibre length have been successful (e.g. Zumberge *et al.* 2002), distributed measurements are still a challenge.

6 CONCLUSIONS

While fibre-optic sensing is still a rapidly emerging technology, cryosphere research has already emerged as a niche where it can make major scientific contributions. Most experiments conducted so far were pilot studies that detected unprecedented amounts of ice quakes, constrained firn and ice structure with metre-scale resolution, produced highly accurate estimates of glacial meltwater runoff, offered insight into the internal structure of snow avalanches or detected previously unobserved phenomena, such as ice sheet resonance and englacial ice quake cascades.

Successful fibre-optic sensing experiments in the cryosphere require more careful planning than in most other environments. Particularly critical field-work issues include the choice and handling of suitable fibre-optic cables, the power supply and setup of DAS interrogators, storage of data volumes in the tens of TB range, splicing in the field at low temperatures, trenching and cable coupling and sensing in both shallow and deep boreholes.

Major remaining science questions are very diverse but are collectively under the umbrella of long-term and large-scale observations of glacial dynamics in the context of a rapidly changing climate. Technical challenges that should be overcome to address these questions involve longer interrogation distances, long-term deployments in more dynamic parts of glaciers, storage and transmission of large data volumes, long-term power supply and absolute strain measurements.

ACKNOWLEDGMENTS

We gratefully acknowledge the careful and constructive comments of editor Duncan Agnew, reviewer Richard Aster and an anonymous reviewer. This paper would be less complete without their help and dedication.

The data and results presented in this paper would not exist without the help of many colleagues who assisted with experimental logistics and field work. We are particularly grateful to Bergur Bergsson, Søren Børsting, Athena Chalari, Malgorzata Chmiel, Yeşim Çubuk-Sabuncu, Dorthe Dahl-Jensen, Pascal Edme, Bergur Einarsson, Olaf Eisen, Andrea Fasciati, Martin Funk, Dominik Gräff, Sverrir Hilmarson, Vala Hjörleifsdóttir, Coen Hofstede, Hildur Jónsdóttir, Kristín Jónsdóttir, Vilhjámur Kjartansson, Sara Klaasen, Manuela Köpfli, Fabian Lindner, Victor Servette, Hlynur Skagfjörd, Anders Svensson, Snaebjörn Sveinsson, Sölvi Thrastarson, Julien Westhoff and Dimitri Zigone. DAS acquisition on Store Glacier was supported by Andy Clarke, Poul Christoffersen, Charlotte Schoonman, Tom Chudley and Robert Law. Borehole drilling and cable installation was led by Bryn Hubbard.

Data acquisition on Grímsvötn was partially funded by the RISE project under the European Union's Horizon 2020 research and innovation programme (grant agreement number 821115) and the IS-TREMOR IRF-grant (grant agreement number 217738).

The Rhône Glacier DAS experiments were supported by the ETH Grants ETH-0616-2 and 1-001179-000, and by the SNF Grants PP00P2_157551 and PP00P2_183719.

DAS acquisition on Store Glacier was funded by the European Research Council as part of the RESPONDER project under the European Union's Horizon 2020 research and innovation program (Grant 683043). Borehole installation was led by Bryn Hubbard, supported by a HERCW/Aberystwyth University Capital Equipment Grant.

EastGRIP and the DAS data acquisition conducted there received funding via the CHIPSM grant of the University of Strasbourg Institute for Advanced Studies and by the French Europe & Foreign Affair ministry and the French Higher Education and Research ministry under the project number 49360YJ–PHC PROCOPE 2023. EastGRIP is directed and organized by the Centre for Ice and Climate at the Niels Bohr Institute, University of Copenhagen. It is supported by funding agencies and institutions in Denmark (A. P. Moller Foundation, University of Copenhagen), the United States (US National Science Foundation, Office of Polar Programs), Germany (Alfred Wegener Institute, Helmholtz Centre for Polar and Marine Research), Japan (National Institute of Polar Research and Arctic Challenge for Sustainability), Norway (University of Bergen and Trond Mohn Foundation), Switzerland (Swiss National Science Foundation), France (French Polar Institute Paul-Emile Victor, Institute for Geosciences and Environmental Research), Canada (University of Manitoba) and China (Chinese Academy of Sciences and Beijing Normal University).

Experiments on Rutford Ice Stream and Skytrain Ice Rise in Antarctica were funded by the NERC Collaborative Antarctic Science Scheme (grant number CASS-166) as part of the BEAMISH project (NERC AFI awards NE/G014159/1 and NE/G013187/1). Rutford surface DAS analysis carried out by T. Hudson, A. Baird and A. Butcher was funded through the Digital Monitoring of CO2

storage project (DigiMon) (project no. 299622), which is part of Accelerating CCS Technologies (ACT) program. The Skytrain Ice Rise borehole and fibre optic cable were part of the University of Cambridge WACSWAIN Project (EU Horizon 2020 agreement no. 742224). Anne Flink, British Antarctic Survey Operations and Rothera Station personnel supported the experiments. The DAS interrogator was loaned from Silixa Ltd with support from Athena Chalari and Andy Clarke.

DATA AVAILABILITY

No new data were generated for this review. A collection of open-source data sets for educational purposes, as described in the main text is available on Zenodo under doi:10.5281/zenodo.12623160 and the title 'Open-access data for "Fibre-optic exploration of the cryosphere"'.

REFERENCES

Acharya, A. & Kogure, T., 2023. Application of novel fibre-optic sensing for slope deformation monitoring: a comprehensive review, *Int. J. Env. Sci. Tech.,* **20,** 8217–8240.

Agnew, D.C. & Wyatt, F.K., 2014. Dynamic strains at regional and teleseismic distances, *Bull. seism. Soc. Am.,* **104**. doi:10.1785/0120140007.

Agrawal, G.P., 2021. *Fiber-Optic Communication Systems,* 5th edn., John Wiley and Sons.

Ajo-Franklin, J.B. *et al.*, 2019. Distributed acoustic sensing using dark fiber for near-surface characterization and broadband seismic event detection, *Sci. Rep.,* **9,** 1328.

Arrowsmith, S.J., Trugman, D.T., MacCarthy, J., Bergen, K.J., Lumley, D. & Magnani, M.B., 2022. Big data seismology, *Rev. Geophys.,* **60**. doi:10.1029/2021RG000769.

Aster, R.C. & Winberry, J.P., 2017. Glacial seismology, *Rep. Prog. Phys.,* **80**. doi:10.1088/1361-6633/aa8473.

Benioff, H., 1935. A linear strain seismograph, *Bull. seism. Soc. Am.,* **25,** 283–309.

Benson, T. *et al.*, 2014. IceCube enhanced hot water drill functional description, *Ann. Glaciol.,* **55**(68), 105–114.

Bernauer, F. *et al.*, 2021. Rotation, strain, and translation sensors performance tests with active seismic sources, *Sensors,* **21,** 264.

Bertholds, A. & Dändliker, R., 1988. Determination of the individual strain-optic coefficients in single-mode optical fibers, *J. Lightwave Tech.,* **6,** 17–20.

Biondi, B., Martin, E., Cole, S., Karrenbach, M. & Lindsey, N., 2017. Earthquake analysis using data recorded by the Stanford DAS array, in *2017 SEG International Exposition and Annual Meeting (SEG-2017-17745041),* SEG, Texas, pp. 2752–1756.

Bogris, A. *et al.*, 2022. Sensitive seismic sensors based on microwave frequency fiber interferometry in commercially deployed cables, *Sci. Rep.,* **12,** 14006.

Booth, A.D. *et al.*, 2020. Distributed acoustic sensing of seismic properties in a borehole drilled on a fast-flowing Greenlandic outlet glacier, *Geophys. Res. Lett.,* **47,** e2020GL088148.

Brisbourne, A.M. *et al.*, 2017. Bed conditions of Pine Island Glacier, West Antarctica, *J. geophys. Res.: Earth Surface,* **122**(1), 419–433.

Brisbourne, A.M., Kendall, M., Kufner, S.K., Hudson, T.S. & Smith, A.M., 2021. Downhole distributed acoustic profiling at the Skytrain Ice Rise, West Antarctica, *The Cryosphere,* **15**. doi:10.5194/tc-15-3443-2021.

Butcher, A., Hudson, T., Kendall, M.J., Kufner, S., Brisbourne, A. & Stork, A., 2021. Radon transform-based detection of microseismicity on DAS networks: a case study from Antarctica, in *EAGE GeoTech 2021 Second EAGE Workshop on Distributed Fibre Optic Sensing,* EAGE, online, pp. 1–4.

Castongia, E., Wang, H.F., Lord, N., Fratta, D., Mondanos, M. & Chalari, A., 2017. An experimental investigation of distributed acoustic sensing (DAS) on Lake Ice, *J. Env. Eng. Geophys.,* **22**. doi:10.2113/Jeeg22.2.167.

Cathles, L.M., Okal, E.A. & MacAyeal, D.R., 2021. Seismic observations of sea swell on the floating Ross Ice Shelf, Antarctica, *J. geophys. Res.,* **114**. doi:10.1029/2007JF000934.

Cheng, F. *et al.*, 2022. Watching the cryosphere thaw: seismic monitoring of permafrost degradation using distributed acoustic sensing during a controlled heating experiment, *Geophys. Res. Lett.,* **49**(10), 1–11.

Chien, C.C. *et al.*, 2025. Calibrating strain measurements: a comparative study of DAS, strainmeter, and seismic data, *Earth Space Sci.,* **12**. doi:10.1029/2024EA003940.

Chmiel, M., Walter, F., Pralong, A., Preiswerk, L., Funk, M., Meier, L. & Brenguier, F., 2023. Seismic constraints on damage growth within an unstable hanging glacier, *Geophys. Res. Lett.,* **50**(9). doi:10.1029/2022GL102007.

Chudley, T.R., Christoffersen, P., Doyle, S.H., Abellan, A. & Snooke, N., 2019. High-accuracy UAV photogrammetry of ice sheet dynamics with no ground control, *Cryosphere,* **13**(3), 955–968.

Cook, J.M., Hodson, A.J. & Irvine-Fynn, T.D., 2016. Supraglacial weathering crust dynamics inferred from cryoconite hole hydrology, *Hydrolog. Process.,* **30**(3), 433–446.

Currenti, G., Jousset, P., Napoli, R., Krawczyk, C. & Weber, M., 2021. On the comparison of strain measurements from fibre optics with a dense seismometer array at Etna volcano (Italy), *Solid Earth,* **12,** 993–1003.

Curtis, A., 1999. Optimal design of focused experiments and surveys, *Geophys. J. Int.,* **139,** 205–215.

Curtis, A. & Maurer, H., 2000. Optimizing the design of geophysical experiments: Is it worthwile?, *The Leading Edge,* **19,** 1058–1062.

Daley, T.M., Pevzner, R., Shulakova, V., Kashikar, S., Miller, D.E., Goetz, J. & ans S. Lueth, J.H., 2013. Field testing of fiber-optic distributed acoustic sensing (DAS) for surbsurface seismic monitoring, *The Leading Edge,* **32,** 936–942.

Daley, T.M., White, D., Miller, D.E., Robertson, M., Freifeld, B., Herkenhoff, F. & Cocker, J., 2014. Simultaneous acquisition of distributed acoustic sensing VSP with multi-mode and single-mode optical cables and 3-component geophones at the Aquistore CO_2 storage site, in *SEG Technical Program Expanded Abstracts (Paper No: segam2014-1357.1),* SEG, pp. 5014–5018.

Daley, T.M., Miller, D.E., Dodds, K., Cook, P. & Freifeld, B.M., 2016. Field testing of modular borehole monitoring with simultaneous distributed acoustic sensing and geophone vertical seismic profiles at Citronelle, Alabama, *Geophys. Prosp.,* **64,** 1318–1334.

Dean, T., Brice, T., Hartog, A., Kragh, E., Molteni, D. & O'Connell, K., 2016. Distributed vibration sensing for seismic acquisition, *The Leading Edge,* **35,** 600–604.

Diez, A., Eisen, O., I. Weikusat, J.E., Hofstede, C., Bohleber, P., Bohlen, T. & Polom, U., 2014. Influence of ice crystal anisotropy on seismic velocity analysis, *Ann. Glaciol.,* **55,** 97–106.

Dong, B., Popescu, A., Tribaldos, V.R., Byna, S., Ajo-Franklin, J. & Wu, K., 2022. Real-time and post-hoc compression for data from distributed acoustic sensing, *Comp. Geosc.,* **166**. doi:10.1016/j.cageo.2022.105181.

Duval, P., Montagnat, M., Grennerat, F., Weiss, J., Meyssonnier, J. & Philip, A., 2010. Creep and plasticity of glacier ice: a material science perspective, *J. Glaciol.,* **56**(200), 1059–1068.

Edme, P., Paitz, P., Walter, F., van Herwijnen, A. & Fichtner, A., 2023. Fiber-optic detection of snow avalanches using telecommunication infrastructure. 12649. doi:10.48550/arXiv.2302.12649.

Ewing, M. & Crary, A.P., 1934. Propagation of elastic waves in ice. Part II, *J. App. Phys.,* **5,** 181–184.

Faillettaz, J., Funk, M. & Vincent, C., 2015. Avalanching glacier instabilities: Review on processes and early warning perspectives, *Rev. Geophys.,* **53**(2), 203–224.

Felikson, D. *et al.*, 2017. Inland thinning on the greenland ice sheet controlled by outlet glacier geometry, *Nat. Geosci.,* **10**(5), 366–369.

Fey, C., Wichmann, V. & Zangerl, C., 2025. Influence of permafrost degradation and glacier retreat on recent high mountain rockfall distribution in the eastern European Alps, *Earth Surf. Process. Landforms,* **50**(5). doi:10.1002/esp.70063.

Fichtner, A. & Hofstede, C., 2023. A simple algorithm for optimal design in distributed fibre-optic sensing, *Geophys. J. Int.,* **233,** 229–233.
Fichtner, A. *et al.*, 2022a. Theory of phase transmission fibre-optic sensing, *Geophys. J. Int.,* **231,** 1233–1248.
Fichtner, A., Klaasen, S., Thrastarson, S., Cubuk-Sabuncu, Y., Paitz, P. & Jonsdottir, K., 2022b. Fiber-optic observation of volcanic tremor through floating ice-sheet resonance, *The Seismic Record,* **2,** 148–155.
Fichtner, A., Hofstede, C., Gebraad, L., Zunino, A., Zigone, D. & Eisen, O., 2023a. Borehole fibre-optic seismology inside the Northeast Greenland Ice Stream, *Geophys. J. Int.,* **235,** 2430–2441.
Fichtner, A., Hofstede, C., Kennett, B.L.N., Nymand, N.F., Lauritzen, M.L., Zigone, D. & Eisen, O., 2023b. Fiber-optic airplane seismology on the Northeast Greenland Ice Stream, *The Seismic Record,* **3,** 125–133.
Fichtner, A. *et al.*, 2025. Hidden cascades of seismic ice stream deformation, *Science,* **387,** 858–864.
Forbriger, T., Karamzadeh, N., Azzola, J., Gaucher, E., Widmer-Schnidrig, R. & Rietbrock, A., 2025. Calibration of the strain amplitude recorded with DAS using a strainmeter array, *Seismol. Res. Lett.,* **96**. doi:10.1785/0220240308.
Gajek, W., Gräff, D., Hellmann, S., Rempel, A.W. & Walter, F., 2021. Diurnal expansion and contraction of englacial fracture networks revealed by seismic shear wave splitting, *Commun. Earth Environ.,* **2**(1), 1–8.
Gräff, D. & Walter, F., 2021. Changing friction at the base of an Alpine glacier, *Sci. Rep.,* **11**(1), 1–10.
Gräff, D. *et al.*, 2025. Calving-driven fjord dynamics resolved by seafloor fibre sensing, *Nature,* **644,** 404–412.
Hartog, A., 2017. *An Introduction to Distributed Optical Fibre Sensors,* CRC Press.
Hill, D., 2015. Distributed Acoustic Sensing (DAS): Theory and Applications , in *Poc. Frontiers in Optics,* Optica Publishing Group, San Jose.
Hornmann, J.C., 2017. Field trial of seismic recording using distributed acoustic sensing with broadside sensitive fibre-optic cables, *Geophys. Prosp.,* **65,** 35–46.
Hudson, T.S. *et al.*, 2021. Distributed Acoustic Sensing (DAS) for natural microseismicity studies: a case study from Antarctica, *J. geophys. Res.,* **126,** e2020JB021493.
Hudson, T.S., Asplet, J. & Walker, A.M., 2023a. Automated shear-wave splitting analysis for single- and multi- layer anisotropic media, *Seismica,* **2**(2). doi:10.26443/seismica.v2i2.1031.
Hudson, T.S., Kufner, S.K., Brisbourne, A.M., Kendall, J.M., Smith, A.M., Alley, R.B., Arthern, R.J. & Murray, T., 2023b. Highly variable friction and slip observed at Antarctic ice stream bed, *Nat. Geosci.,* **16**(7), 612–618.
Hudson, T.S., Klaasen, S.A., Fontaine, O., Bacon, C.A., Jónsdóttir, K. & Fichtner, A., 2025. Towards a widely applicable earthquake detection algorithm for fibreoptic and hybrid fibreoptic-seismometer networks, *Geophys. J. Int.,* **240**. doi:10.1093/gji/ggae459.
Huss, M., Dhulst, L. & Bauder, A., 2015. New long-term mass-balance series for the Swiss Alps, *J. Glaciol.,* **61**(227), 551–562.
Igel, J., Klaasen, S., Noe, S., Nomikou, P., Karantzalos, K. & Fichtner, A., 2024. Challenges in submarine fiber-optic earthquake monitoring, *ESS Open Archive,* e2024JB029556. doi:10.22541/essoar.171691177.74747140/v1.
Iken, A., 1988. Adaption of the hot-water-drilling method for drilling to great depth, *Mitteilungen der Versuchsanstalt fur Wasserbau, Hydrologie und Glaziologie an der Eidgenossischen Technischen Hochschule Zurich,* **19**(94), 211–229.
IPCC, 2023. Climate Change 2023: Synthesis Report. Contribution of Working Groups I, II and III to the Sixth Assessment Report of the Intergovernmental Panel on Climate Change, in , Core Writing Team, Lee, H. & Romero, J.(eds.), IPCC, Geneva, Switzerland, p. 184.
Issah, A.H.S. & Martin, E.R., 2024. Impact of lossy compression errors on passive seismic data analysis, *Seis. Res. Lett.,* **95**. doi:10.1785/0220230314.
Joughin, I., Alley, R.B. & Holland, D.M., 2012. Ice-Sheet Response to Oceanic Forcing, *Science,* **338**(6111), 1172–1176.
Joughin, I., Smith, B.E. & Schoof, C.G., 2019. Regularized Coulomb friction laws for ice sheet sliding: application to Pine Island Glacier, Antarctica, *Geophys. Res. Lett.,* **46,** 4764–4771.
Jousset, P. *et al.*, 2022. Fibre optic distributed acoustic sensing of volcanic events, *Nat. Comm.,* **13,** 1753.
Jousset, P. *et al.*, 2025. Fiber optic sensing for volcano monitoring and imaging volcanic processes, *Modern Volcano Monitoring, Advances in Volcanology,* pp. 509–567, eds Spica, Z. & Caudron, C., Spring Nature.
Kennett, B.L.N., 2024. *A Guide to the Seismic Wavefield as seen by DAS,* The Australian National University.
Kennett, B.L.N., Lai, V.H., Miller, M.S., Bowden, D.C. & Fichtner, A., 2024. Near-source effects on DAS recording: implications for tap tests, *Geophys. J. Int.,* **237,** 436–444.
Klaasen, S., Paitz, P., Lindner, N., Dettmer, J. & Fichtner, A., 2021. Distributed Acoustic Sensing in volcano-glacial environments—Mount Meager, British Columbia, *J. geophys. Res.: Solid Earth,* **126,** e2021JB022358.
Klaasen, S., Thrastarson, S., Fichtner, A., Cubuk-Sabuncu, Y. & Jonsdottir, K., 2022. Sensing Iceland's most active volcano with a "buried hair", *EOS, Trans. Am. geophys. Un.,* **103**. doi:10.1029/2022EO220007.
Klaasen, S., Thrastarson, S., Cubuk-Sabuncu, Y., Jonsdottir, K., Gebraad, L., Paitz, P. & Fichtner, A., 2023. Subglacial volcano monitoring with fiber-optic sensing: Grímsvötn, Iceland, *Volcanica,* **6,** 301–311.
Kleine, F., Bruland, C., Wüstefeld, A., Oye, V. & Landro, M., 2025. Seismic signal classification of snow avalanches using Distributed Acoustic Sensing in Grasdalen, Western Norway, *Nat. Haz. Earth Sys. Sci. Discuss.,* **25,** 2771–2782.
Kochtitzky, W. *et al.*, 2022. The unquantified mass loss of Northern Hemisphere marine-terminating glaciers from 2000–2020, *Nat. Commun.,* **13**(1), 1–10.
Kohnen, H., 1972. Über die Beziehung zwischen seismischen Geschwindigkeiten und der Dichte in Firn und Eis, *Z. Geophys,* **38,** 925–935.
Kufner, S.K., Wookey, J., Brisbourne, A.M., Martín, C., Hudson, T.S., Kendall, J.M. & Smith, A.M., 2023. Strongly depth-dependent ice fabric in a fast-flowing Antarctic ice stream revealed with icequake observations, *J. geophys. Res.: Earth Surface,* **128**(3), 1–25.
Kuvshinov, B.N., 2015. Interaction of helically wound fibre-optic cables with plane seismic waves, *Geophys. Prosp.,* **64,** 671–688.
Lai, C.Y., Kingslake, J., Wearing, M.G., Chen, P.h.C., Gentine, P., Li, H., Spergel, J.J. & van Wessem, J.M., 2020. Vulnerability of Antarctica's ice shelves to meltwater-driven fracture, *Nature,* **584**(7822), 574–578.
Lanteri, A. *et al.*, 2025. Seismic constraints on glacier density, *Sci. Rep.,* **15**. doi:10.1038/s41598-025-26440-z.
Lapins, S., Butcher, A., Kendall, J.M., Hudson, T.S., Stork, A.L., Werner, M.J., Gunning, J. & Brisbourne, A.M., 2024. DAS-N2N: machine learning distributed acoustic sensing (DAS) signal denoising without clean data, *Geophys. J. Int.,* **236,** 1026–1041.
Leung, J., Hudson, T.S., Kendall, J.M. & Barcheck, G., 2025. Evidence that seismic anisotropy captures upstream palaeo-ice fabric: implications on present-day deformation at Whillans Ice Stream, Antarctica, *J. Glaciol.,* **71,** e39. doi:10.1017/jog.2025.19.
Lindner, F., Wassermann, J. & Igel, H., 2021. Seasonal freeze-thaw cycles and permafrost degradation on Mt. Zugspitze (German/Austrian Alps) revealed by single-station seismic monitoring, *Geophys. Res. Lett.,* **48**(18), 1–11.
Lindner, F., Smolinski, K.T., Scandroglio, R., Fichtner, A. & Wassermann, J., 2025. *Permafrost Distribution and Hydrostatic Pore Pressure at Mt. Zugspitze (German/Austrian Alps): Insights from Seismology including DAS*. doi:10.22541/essoar.174858326.63410461/v1.
Lindsey, N.J. & Martin, E., 2021. Fiber-optic seismology, *Ann. Rev. Earth Plant. Sci.,* **49,** 309–336.
Lindsey, N.J., Martin, E.R., Dreger, D.S., Freifeld, B., Cole, S., James, S.R., Biondi, B.L. & Ajo-Franklin, J.B., 2017. Fiber-optic network observations of earthquake wavefields, *Geophys. Res. Lett.,* **44,** 11 792–11 799.
Lindsey, N.J., Rademacher, H. & Ajo-Franklin, J.B., 2020. On the broadband instrument response of fiber-optic DAS arrays, *J. geophys. Res.,* **125,** doi:doi:10.1029/2019JB018145.

Lior, I. *et al.*, 2021. On the detection capabilities of underwater distributed acoustic sensing, *J. geophys. Res.: Solid Earth,* **126**(3), e2020JB020925. doi:10.1029/2020JB020925.

Manos, J.M., Gräff, D., Martin, E., Paitz, P., Walter, F., Fichtner, A. & Lipovsky, B.P., 2024. DAS to discharge: using distributed acoustic sensing (DAS) to infer glacier runoff, *J. Glaciol.,* **70,** e67. doi:10.1017/jog.2024.46.

Marra, G. *et al.*, 2018. Ultrastable laser interferometry for earthquake detection with terrestrial and submarine cables, *Science,* **361,** 486–490.

Martin, E.R., Castillo, C.M., Cole, S., Sawasdee, P.S., Yuan, S., Clapp, R., Karrenbach, M. & Biondi, B.L., 2017. Seismic monitoring leveraging existing telecom infrastructure at the SDASA: Active, passive, and ambient-noise analysis, *The Leading Edge,* **36,** 1025–1031.

Mateeva, A. *et al.*, 2013. Distributed acoustic sensing for reservoir monitoring with VSP, *The Leading Edge,* **32,** 1278–1283.

Mateeva, A. *et al.*, 2014. Distributed acoustic sensing for reservoir monitoring with vertical seismic profiling, *Geophys. Prosp.,* **62,** 679–692.

Maurer, H., Nuber, A., Korta Martiartu, N., Reiser, F., Boehm, C., Manukyan, E., Schmelzbach, C. & Fichtner, A., 2017. Optimized experimental design in the context of seismic full waveform inversion and seismic waveform imaging, *Adv. Geophys.,* **58,** 1–45.

Mecozzi, A., Cantono, M., Castellanos, J.C., Kamalov, V., Muller, R. & Zhan, Z., 2021. Polarization sensing using submarine optical cables, *Optica,* **8,** 788–794.

Meylan, M.H., Ilyas, M., Lamichhane, B.P. & Bennetts, L.G., 2021. Swell-induced flexural vibrations of a thickening ice shelf over a shoaling seabed, *Proc. R. Acad. Sci. A,* **477**. doi:10.1098/rspa.2021.0173.

Miner, K.R. *et al.*, 2022. Permafrost carbon emissions in a changing Arctic, *Nat. Rev. Earth and Environ.,* **3**(1), 55–67.

Muto, A., Alley, R.B., Parizek, B.R. & Anandakrishnan, S., 2019. Bed-type variability and till (dis)continuity beneath Thwaites Glacier, West Antarctica, *Ann. Glaciol.,* **60**(80), 82–90.

Ni, Y. *et al.*, 2025. A Review of Cloud Computing in Seismology *Geophys. j. Int.,* **243**(1), ggaf322. doi:10.1093/gji/ggaf322.

Ning, I.L.C. & Sava, P., 2018. Multicomponent distributed acoustic sensing: Concept and theory, *Geophysics,* **83**. doi:10.1190/geo2017-0327.1.

Nolan, M. & Echelmeyer, K., 1999. Seismic detection of transient changes beneath black rapids glacier, Alaska, USA: I. techniques and observations, *J. Glaciol.,* **45**(149), 119–131.

Nye, J.F., 1957. *Physical Properties of Crystals,* Oxford Clarendon Press.

Nziengui-Bâ, D., Coutant, O., Moreau, L. & Boué', P., 2023. Measuring the thickness and young's modulus of the ice pack with DAS, a test case on a frozen mountain lake, *Geophys. J. Int.,* **233,** 1166–1177.

Ockenden, H., Bingham, R.G., Curtis, A. & Goldberg, D., 2022. Inverting ice surface elevation and velocity for bed topography and slipperiness beneath Thwaites Glacier, *Cryosphere,* **16**(9), 3867–3887.

Oliver, J., Crary, A.P. & Cotell, R., 1954. Elastic waves in Arctic pack ice, *EOS, Trans. Am. Geophys. Un.,* **35,** 282–292.

Oppenheimer, M. *et al.*, 2019. Sea Level Rise and Implications for Low-Lying Islands, Coasts and Communities, in *IPCC Special Report on the Ocean and Cryosphere in a Changing Climate,* IPCC, pp. 321–445.

Ouellet, S.M. *et al.*, 2024. Previously hidden landslide processes revealed using distributed acoustic sensing with nanostrain-rate sensitivity, *Nat. Comm.,* **15**. doi:10.1038/s41467-024-50604-6.

Owen, A., Duckworth, G. & Worsley, J., 2012. Fibre-optic distributed acoustic sensing for border monitoring, in *EISIC '12: Proceedings of the 2012 European Intelligence and Security Informatics Conference,* IEEE Computer Society, Washington.

Paitz, P., Edme, P., Gräff, D., Walter, F., Doetsch, J., Chalari, A., Schmelzbach, C. & Fichtner, A., 2021. Empirical investigations of the instrument response for distributed acoustic sensing (DAS) across 17 octaves, *Bull. seism. Soc. Am.,* **111,** 1–10.

Paitz, P., Lindner, N., Edme, P., Huguenin, P., Hohl, M., Sovilla, B., Walter, F. & Fichtner, A., 2023. Phenomenology of avalanche recordings from distributed acoustic sensing, *J. geophys. Res.,* **128,** e2022JF007011.

Paterson, W.S.B., 1994. *Physics of Glaciers,* Butterworth-Heinemann.

Peña Castro, A.F., Schmandt, B., Baker, M.G. & Abbott, R.E., 2023. Tracking local sea ice extent in the Beaufort sea using distributed acoustic sensing and machine learning, *Seismic Record,* **3**(3), 200–209.

Pfeffer, W., 2007. A simple mechanism for irreversible tidewater glacier retreat, *J. geophys. Res.: Earth Surface,* **112**. doi:10.1029/2006JF000590.

Podolskiy, E.A. & Walter, F., 2016. Cryoseismology, *Rev. Geophys.,* **54,** 708–758.

Pollard, D., DeConto, R.M. & Alley, R.B., 2015a. Potential Antarctic Ice Sheet retreat driven by hydrofracturing and ice cliff failure, *Earth planet. Sci. Lett.,* **412,** 112–121.

Pollard, D., DeConto, R.M. & Alley, R.B., 2015b. Potential Antarctic ice sheet retreat driven by hydrofracturing and ice cliff failure, *Earth planet. Sci. Lett.,* **412,** 112–121.

Press, F. & Ewing, M., 1951. Propagation of elastic waves in a floating ice sheet, *EOS, Trans. Am. Geophys. Un.,* **32,** 673–678.

Riel, B., Minchew, B. & Bischoff, T., 2021. Data-Driven Inference of the Mechanics of Slip Along Glacier Beds Using Physics-Informed Neural Networks, *J. Adv. Model. Earth Syst.,* **13**. doi:10.1029/2021MS002621.

Riesen, P., Sugiyama, S. & Funk, M., 2010. The influence of the presence and drainage of an ice-marginal lake on the flow of gornergletscher, switzerland, *J. Glaciol.,* **56**(196), 278–286.

Rost, S. & Thomas, C., 2002. Array seismology: Methods and applications, *Rev. Geophys.,* **40,** 1008.

Ryser, C., Lüthi, M., Blindow, N., Suckro, S., Funk, M. & Bauder, A., 2013. Cold ice in the ablation zone: Its relation to glacier hydrology and ice water content, *J. geophys. Res.: Earth Surface,* **118**(2), 693–705.

Schwikowski, M., Jenk, T.M., Stampfli, D. & Stampfli, F., 2014. A new thermal drilling system for high-altitude or temperate glaciers, *Ann. Glaciol.,* **55**(68), 131–136.

Segui, A., Ugalde, A., Fichtner, A., Ventosa, S. & Morros, J.R., 2025. DASPack: Controlled data compression for Distributed Acoustic Sensing, *Geophys. J. Int.,* **244**. doi:10.1093/gji/ggaf397.

Seroussi, H. *et al.*, 2024. Evolution of the Antarctic Ice Sheet over the next three centuries from an ISMIP6 model ensemble, *Earth's Future,* **12**. doi:10.1029/2024EF004561.

Sheldon, S.G., Steffensen, J.P., Hansen, S.B., Popp, T.J. & Johnsen, S.J., 2014. The investigation and experience of using ESTISOL^{TM}240 and COASOL^{TM}for ice-core drilling, *Ann. Glaciol.,* **55,** 219–232.

Sidenko, E., Tertyshnikov, K., Lebedev, M. & Pevzner, R., 2022. Experimental study of temperature change effect on distributed acoustic sensing continuous measurements, *Geophysics,* **87**. doi:10.1190/GEO2021-0524.1.

Singh, V., McCarthy, C., Silvia, M., Jakuba, M.V., Craft, K.L., Rhoden, A.R., German, C. & Koczynski, T.A., 2023. Surviving in ocean worlds: experimental characterization of fiber optic tethers across europa-like ice faults and unraveling the sliding behavior of ice, *Planet. Sci. J.,* **4**. doi:10.3847/PSJ/aca3ab.

Sladen, A., Rivet, D., Ampuero, J.P., De Barros, L., Hello, Y., Calbris, G. & Lamare, P., 2019. Distributed sensing of earthquakes and ocean-solid Earth interactions on seafloor telecom cables, *Nat. Commun.,* **10**(1), 5777. doi:10.1038/s41467-019-13793-z.

Smith, E.C., Baird, A.F., Kendall, J.M., Martin, C., White, R.S., Brisbourne, A.M. & Smith, A.M., 2017. Ice fabric in an Antarctic ice stream interpreted from seismic anisotropy, *Geophys. Res. Lett.,* **44**(8), 3710–3718.

Smith, M.M., Thomson, J., Baker, M.G., Abbott, R.E. & Davis, J., 2023. Observations of ocean surface wave attenuation in sea ice using seafloor cables, *Geophys. Res. Lett.,* **50**(20). doi:10.1029/2023GL105243.

Smolinski, K., Bowden, D., Paitz, P., Kugler, F. & Fichtner, A., 2024. Shallow subsurface imaging using challenging urban DAS data, *Seis. Res. Lett.,* **2024**. doi:10.1785/0220240052.

Spica, Z.J., Nishida, K., Akuhara, T., Petrelis, F., Shinohara, M. & Yamada, T., 2020a. Marine sediment characterized by ocean-bottom fiber-optic seismology, *Geophys. Res. Lett.,* **47,** e2020GL088360.

Spica, Z.J., Perton, M., Martin, E.R., Beroza, B.C. & Biondi, B., 2020b. Urban seismic site characterization by fiber-optic seismology, *J. geophys. Res.,* **125,** e2019JB018656.

Talalay, P., Fan, X., Xu, H., Yu, D., Han, L., Han, J. & Sun, Y., 2014. Drilling fluid technology in ice sheets: hydrostatic pressure and borehole closure considerations, *Cold Regions Sci. Technol.,* **98,** 47–54.

Teanby, N.A., Kendall, J. & Baan, M.V.D., 2004. Automation of shear-wave splitting measurements using cluster analysis, *Bull. seism. Soc. Am.,* **94**(2), 453–463.

Turquet, A., Wuestefeld, A., Svendsen, G.K., Nyhammer, F.K., Nilsen, E.L., Persson, A.P.O. & Refsum, V., 2024. Automated snow avalanche monitoring and alert system using distributed acoustic sensing, *GeoHazards,* **5,** 1326–1345.

Waagaard, O.H., Rønnekleiv, E., Haukanes, A., Stabo-Eeg, F., Thingbø, D., Forbord, S., Aasen, S.E. & K., J., 2021. Real-time low noise distributed acoustic sensing in 171 km low loss fiber, *OSA Continuum,* **4,** 688–701.

Walter, F., Gräff, D., Lindner, F., Paitz, P., Köpfli, M., Chmiel, M. & Fichtner, A., 2020. Distributed Acoustic Sensing of microseismic sources and wave propagation in glaciated terrain, *Nat. Comm.,* **11**. doi:10.1038/s41467-020-15824.

Weertman, J., 1974. Stability of the Junction of an Ice Sheet and an Ice Shelf, *J. Glaciol.,* **13**(67), 3–11.

Werder, M.A., Hewitt, I.J., Schoof, C.G. & Flowers, G.E., 2013. Modeling channelized and distributed subglacial drainage in two dimensions, *J. geophys. Res.: Earth Surface,* **118**(4), 2140–2158.

Williams, E.F., Fernández-Ruiz, M.R., Magalhaes, R., Vanthillo, R., Zhan, Z., González-Herráez, M. & Martins, H.F., 2019. Distributed sensing of microseisms and teleseisms with submarine dark fibers, *Nat. Commun.,* **10**(1), 1–11.

Willis, R.M. *et al.*, 2025. Creating a comprehensive cryoseismic catalog at Rhonegletscher: a scalable approach using Distributed Acoustic Sensing and Machine Learning, *J. geophys. Res.,* in press.

Xie, J. *et al.*, 2024. Ice plate deformation and cracking revealed by an *in situ*-distributed acoustic sensing array, *The Cryosphere,* **18,** 837–847.

Yang, Y., Zhan, Z., Karrenbach, M., Reid-McLaughlin, A., Biondi, E., Wiens, D.A. & Aster, R.C., 2024. Characterizing south pole firn structure with fiber optic sensing, *Geophys. Res. Lett.,* **51**. doi:10.1029/2024GL109183.

Zhan, Z., 2020. Distributed acoustic sensing turns fiber-optic cables into sensitive seismic antennas, *Seis. Res. Lett.,* **91,** 1–15.

Zhou, W., Butcher, A., Brisbourne, A., Kufner, S.K., Kendall, J.M. & Stork, A., 2022. Seismic noise interferometry and Distributed Acoustic Sensing (DAS): measuring the firn layer *S*-velocity structure on Rutford Ice Stream, Antarctica, *J. geophys. Res.,* **127**. doi:10.1029/2022JF006917.

Zitt, J., Paitz, P., Fichtner, A., Walter, F. & Umlauft, J., 2025. Self-supervised coherence-based denoising of cryoseismological Distributed Acoustic Sensing data, *J. geophys. Res. - Mach. Learn. Comp.,* **2**. doi:10.1029/2024JH000414.

Zoet, L.K., Anandakrishnan, S., Alley, R.B., Nyblade, A.A. & Wiens, D.A., 2012. Motion of an Antarctic glacier by repeated tidally modulated earthquakes, *Nat. Geosci.,* **5**(9), 623–626.

Zumberge, M.A., Elsberg, D.H., Harrison, W.D., Husmann, E., Morack, J.L., Pettit, E.C. & Waddington, E.D., 2002. Measurement of vertical strain and velocity at Siple Dome, Antarctica, with optical sensors, *J. Glaciol.,* **48**. doi:10.3189/172756502781831421.

APPENDIX A: OPEN DATA SETS AND ANALYSIS TOOLS

Storage formats of DAS recordings, the nature of the data and the methods used to analyse them vary widely. On the one hand, this is due to the absence of a widely accepted standard format. On the other hand, it results from the diversity of observable phenomena and DAS interrogators that preclude the existence of a one-fits-all solution.

The open-access collection of cryospheric DAS data sets, enclosed in this publication, is intended to reflect part of this diversity and to provide an opportunity for hands-on training and experimentation with actual field data. Most of the data sets have already been described in the signal gallery of Section 4. These include the active-source borehole data from Store Glacier (Fig. 9, Booth *et al.* 2020), surface crevassing and stick-slip events from Rhône Glacier (Fig. 10c, Walter *et al.* 2020), stick-slip events from Rutford Ice Stream (Fig. 11, Hudson *et al.* 2021), cascading englacial icequakes in the Northeast Greenland Ice Stream (Fig. 12, Fichtner *et al.* 2025) and the snow avalanche recordings from the Vallée de la Sionne (Fig. 16a, Paitz *et al.* 2023). Additional data sets are described below.

A1 Recording of multimode surface waves from an airplane landing

This data set, illustrated in Fig. A1, was recorded on 2022 July 26 near the camp of the East Greenland Ice Core Project (EastGRIP) on the Northeast Greenland Ice Stream (Fichtner *et al.* 2023b). The wavefield was excited by the landing of a C-130 Hercules airplane at a small angle of a 2500 m long straight segment of a fibre-optic cable, trenched with the help of a snow cat ∼0.5 m into the firn. While the time-domain recordings are complex, the frequency-phase velocity version reveals multiple clearly defined wave propagation modes, including the fundamental-mode Rayleigh wave, numerous Rayleigh overtones, a leaky mode and several pseudo-acoustic (trapped *P* wave) modes. The unusually large number of modes, combined with the high data quality, provides tight constraints on the structure of the firn layer within the upper ∼100 m of the ice sheet.

A2 Recording near-surface crevassing at an Alpine glacier using a dense surface fibre-optic array

Fig. A2 shows an example data set from Gorner Glacier, an Alpine glacier in Switzerland. The novelty of this data set lies in deploying a dense 2-D fibre geometry over an active crevasse field. The interrogator was located off the ice to minimize surface-wave noise from a generator used to power the interrogator. Fibre was laid parallel and perpendicular to crevasses, directly on the ice surface. The deployment was timed to occur just as the weather conditions transitioned to sub-zero temperatures, allowing the fibre to melt in and then freeze into the ice. This resulted in good coupling of the majority of channels, with the exception of channels traversing crevasses (see Fig. A2c, for example). Effects of this poor coupling can be seen in the plot of strain with distance along the fibre through time (Fig. A2d). Fig. A2(d) also shows an example of an ice quake caused by near-surface crevassing. A *P* wave can clearly be observed, followed by a higher amplitude dispersive surface wave arrival. These arrivals can clearly be identified in individual channel traces (Fig. A2e). A further feature of interest is the strong coda signal after the surface wave arrival. This is likely caused by scattering of surface waves off the numerous crevasses, possibly combined with meltwater resonances in some of the crevasses (e.g. see signals at ∼ 400 and ∼ 1000 m following the surface-wave arrival).

A3 Recording hammer and plate signals at an Antarctic ice core site with partial fluid-fill

Fig. A3 introduces a borehole DAS experiment conducted at Skytrain Ice Rise in West Antarctica (Brisbourne *et al.* 2021). The fibre-optic cable was deployed a year earlier following ice core retrieval with the aim of measuring the temperature of the ice column using distributed temperature sensing. The hole was left approximately half-filled with drilling fluid. The upper half of the cable was therefore suspended in air with only the lower half suspended

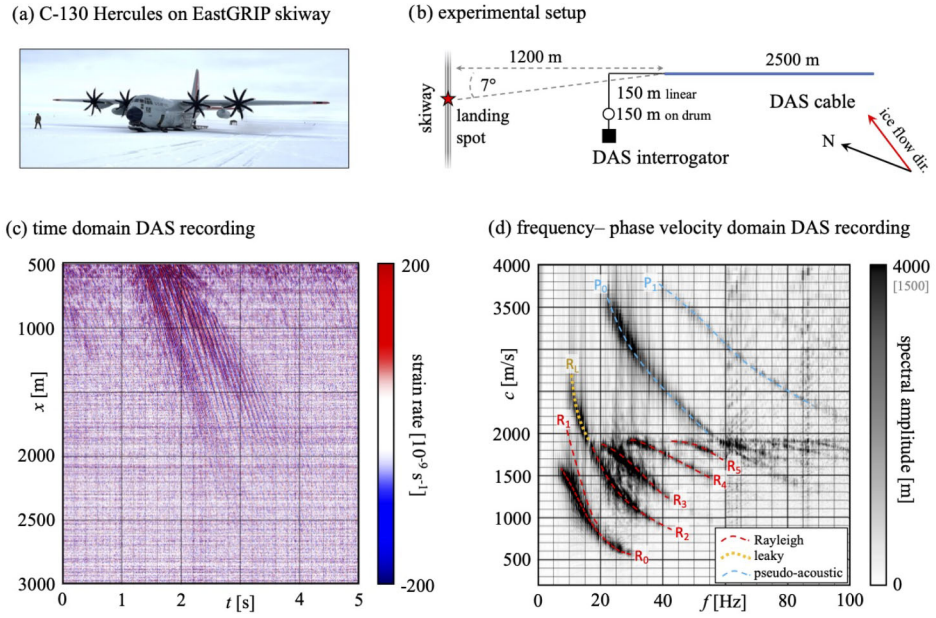

Figure A1. Airplane landing data. (a) Photograph of the C-130 Hercules, shortly after landing near the EastGRIP camp. (b) Geometry of the 3000 m long fibre-optic cable. The last ∼2500 m are nearly straight, forming an angle of ∼ 7° to the estimated landing spot. (c) Time-domain DAS recordings on the last 2500 m of the cable. (d) Amplitude spectrum of the data in the frequency–phase velocity domain. Marked features include multiple Rayleigh modes (R_i), a leaky mode (R_L) and pseudo-acoustic modes (P_0). Frequencies above 60 Hz are shown with a lower colour bar saturation, for better visibility.

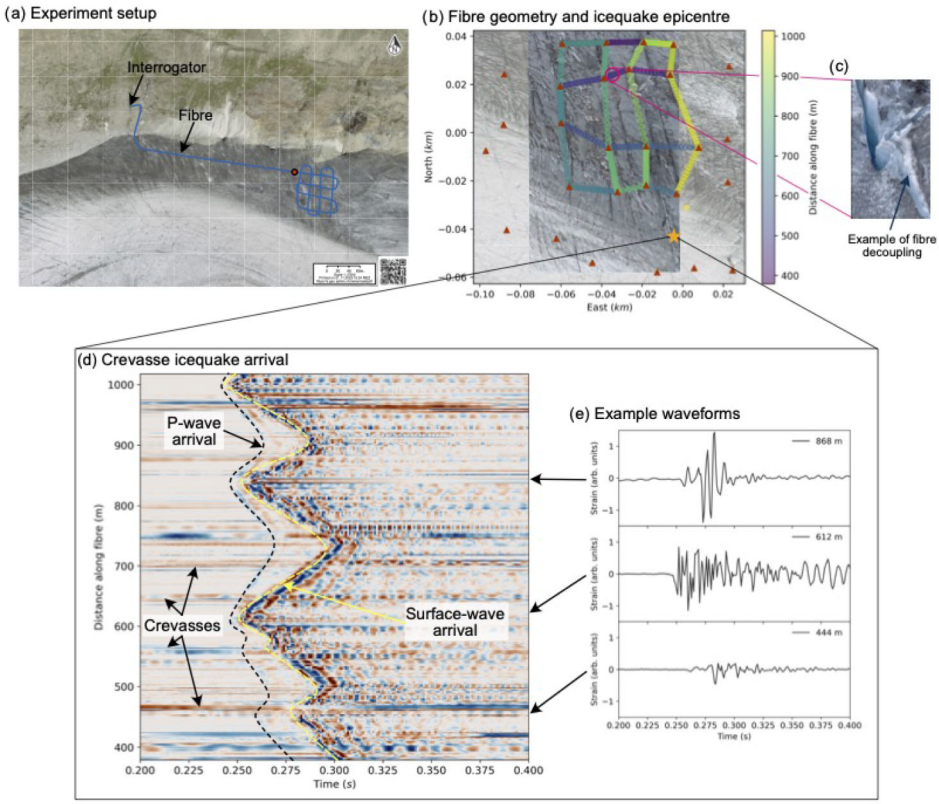

Figure A2. Alpine glacier crevasse field data (Gorner Glacier, Switzerland). (a) Experiment setup. (b) Detailed fibre geometry and ice quake location (orange star). Red triangles are single-component seismic nodes. (c) Example of how the fibre is decoupled from the ice when crossing a crevasse. (d) Example of a DAS record section for a crevasse ice quake. (e) Examples of waveforms of selected DAS channels. The aerial imagery in (a) and (b) is from the Swiss Federal Office of Topography (Swisstopo).

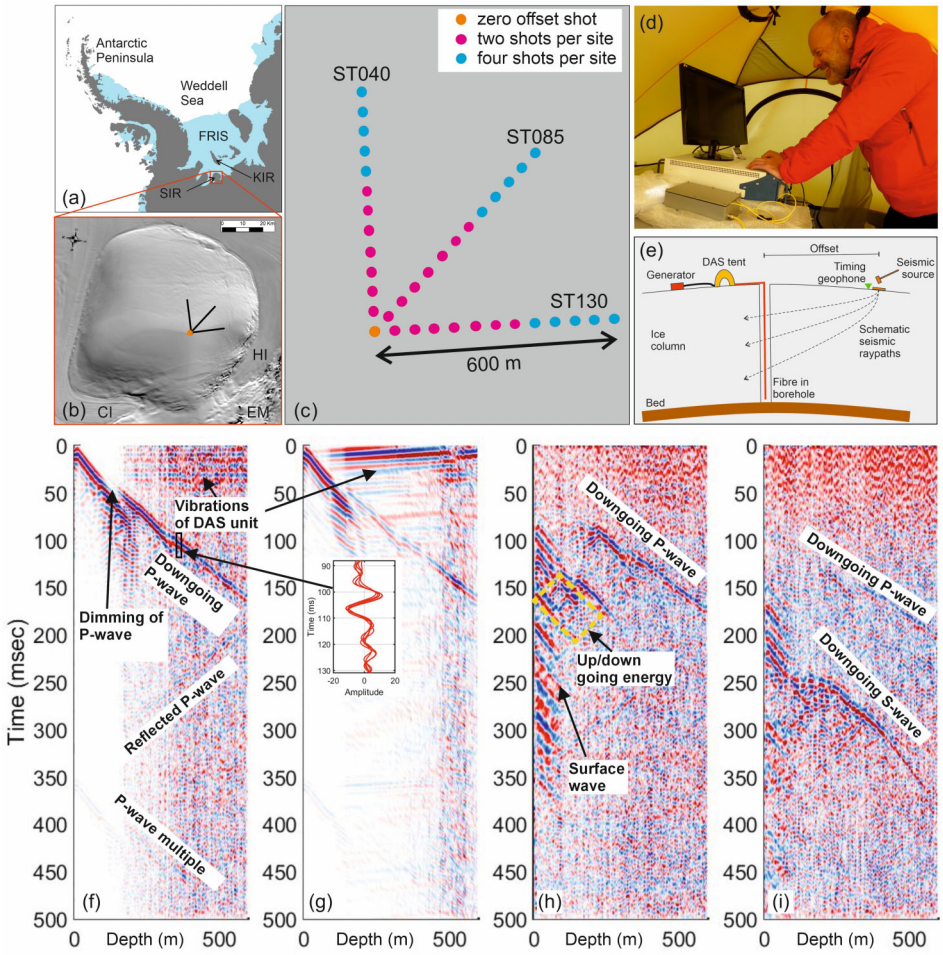

Figure A3. (a) Location of the experiment on Skytrain Ice Rise (SIR) in West Antarctica. FRIS–Filchner–Ronne Ice Shelf; KIR–Korff Ice Rise. (b) Orientation of walkaway hammer and plate seismic lines on SIR (not to scale). The background is MODIS imagery. HI–Hercules Inlet; CI–Constellation Inlet; EM–Ellsworth–Whitmore Mountains. (c) Scale map of shot locations with respect to the borehole at 79 44.50 S, 078 32.70W (orange dot). Line names reference the orientation with respect to magnetic north. (d) DAS interrogator in a mountain tent. (e) Schematic of acquisition illustrating the key components of the field set-up. (f–i) Example DAS VSPs along line ST130 with signal and noise labelled. Traces are normalized at each depth to highlight coherent arrivals. This also results in the dimming of signals over depths with high amplitude arrivals dominating. (f) Primary, reflected and surface multiple *P* waves at zero offset with a bandpass filter of 2–140 Hz. Vibrations from the generator and wind noise of the DAS interrogator appear as horizontal lines in these sections. The apparent dimming of the *P* wave at 50 ms is due to the high amplitudes of the following signals. (g) Downgoing *P*-wave energy at zero offset isolated using an f–k filter and adaptive deconvolution to remove upgoing energy and reduce coherent noise. Some upgoing energy is preserved due to the taper used on the f–k filter. Inset: example waveforms of five downgoing *P* waves at 100 ms and 350 m depth, indicated by the black box in (f) (no f–k filter applied). (h) Source at 200 m offset with a bandpass filter of 2–140 Hz. The characteristic diamond-pattern is highlighted by the dashed yellow box. (i) Both *P*-wave and *S*-wave arrivals are visible at 400 m source offset with a bandpass filter of 2–140 Hz applied.

in the fluid. Walkaway vertical seismic profiles were acquired at three azimuths using a sledgehammer and a rigid plate. Repeated hammer blows were acquired to allow stacking. Coherent noise on the DAS unit itself results from the power generator and strong winds. Noise on the undamped fibre suspended in air is significant at shallow depths. However, with the source located at near offsets, where ray paths are parallel to the cable, down-going (direct), up-going (ice-bed reflection) and surface-multiple *P* waves are visible. With sources at greater offsets, and ray paths therefore oblique to the cable, down-going *S* waves are observed.